Geoscientific
Model Development

MOPSMAP v1.0: a versatile tool for the modeling of aerosol optical properties

Josef Gasteiger[1] and **Matthias Wiegner**[2]

[1]Faculty of Physics, University of Vienna, Vienna, Austria
[2]Meteorologisches Institut, Ludwig-Maximilians-Universität, Munich, Germany

**Correspondence:** Josef Gasteiger (josef.gasteiger@univie.ac.at)

Abstract. The spatiotemporal distribution and characterization of aerosol particles are usually determined by remote-sensing and optical in situ measurements. These measurements are indirect with respect to microphysical properties, and thus inversion techniques are required to determine the aerosol microphysics. Scattering theory provides the link between microphysical and optical properties; it is not only needed for such inversions but also for radiative budget calculations and climate modeling. However, optical modeling can be very time-consuming, in particular if nonspherical particles or complex ensembles are involved.

In this paper we present the MOPSMAP package (Modeled optical properties of ensembles of aerosol particles), which is computationally fast for optical modeling even in the case of complex aerosols. The package consists of a data set of pre-calculated optical properties of single aerosol particles, a Fortran program to calculate the properties of user-defined aerosol ensembles, and a user-friendly web interface for online calculations. Spheres, spheroids, and a small set of irregular particle shapes are considered over a wide range of sizes and refractive indices. MOPSMAP provides the fundamental optical properties assuming random particle orientation, including the scattering matrix for the selected wavelengths. Moreover, the output includes tables of frequently used properties such as the single-scattering albedo, the asymmetry parameter, or the lidar ratio. To demonstrate the wide range of possible MOPSMAP applications, a selection of examples is presented, e.g., dealing with hygroscopic growth, mixtures of absorbing and non-absorbing particles, the relevance of the size equivalence in the case of nonspherical particles, and the variability in volcanic ash microphysics.

The web interface is designed to be intuitive for expert and nonexpert users. To support users a large set of default settings is available, e.g., several wavelength-dependent refractive indices, climatologically representative size distributions, and a parameterization of hygroscopic growth. Calculations are possible for single wavelengths or user-defined sets (e.g., of specific remote-sensing application). For expert users more options for the microphysics are available. Plots for immediate visualization of the results are shown. The complete output can be downloaded for further applications. All input parameters and results are stored in the user's personal folder so that calculations can easily be reproduced. The web interface is provided at https://mopsmap.net (last access: 9 July 2018) and the Fortran program including the data set is freely available for offline calculations, e.g., when large numbers of different runs for sensitivity studies are to be made.

1 Introduction

Aerosol particles in the Earth's atmosphere are important in various ways, for example because of their interaction with electromagnetic radiation and their effect on cloud properties. Consequently aerosol particles are relevant for weather and climate. The temporal and spatial variability in their abundance as well as the variability in their properties is significant which poses huge challenges in quantifying their effects. This includes the need to establish extended networks of observations using instruments such as photometers (Holben et al., 1998), lidars (Pappalardo et al., 2014), or ceilometers (Wiegner et al., 2014) and the development of models
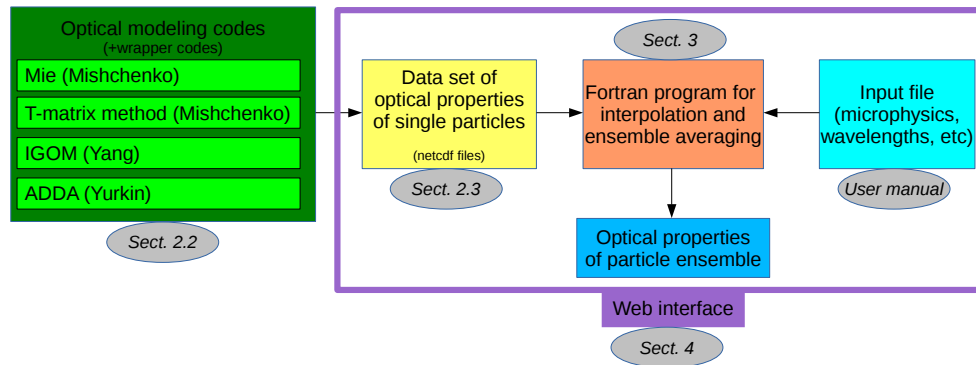
Figure 1. Scheme of the MOPSMAP package, including the optical modeling codes applied to create the data set.

to predict the influence of particles on the state of the atmosphere; see, e.g., Baklanov et al. (2014).

Aerosol properties and distributions are often quantified by ground-based and spaceborne optical remote sensing and by optical in situ measurements. These measurements are indirect with respect to microphysical properties (e.g., particle size) because they measure optical quantities and require the application of inversion techniques to retrieve microphysical properties. Precise knowledge on the link between microphysical and optical properties is needed for the inversion. This link is provided by optical modeling, i.e., the optical properties of particles are calculated based on their microphysical properties. Optical modeling is required also for other applications, e.g., for radiative transfer, numerical weather prediction, and climate modeling. As optical modeling can be very time-consuming, it is often inevitable to pre-calculate optical properties of particles and store them in a lookup table, which is then accessed by the inversion procedures or subsequent models.

In our contribution we describe the MOPSMAP (Modeled optical properties of ensembles of aerosol particles) package, which consists of a data set of pre-calculated optical properties of single aerosol particles, a Fortran program which calculates the properties of user-defined aerosol ensembles from this data set, and a user-friendly web interface for online calculations. Figure 1 illustrates the overall scheme of the package, including the optical modeling codes (green box) needed once to prepare the underlying data set. MOPSMAP is either provided via an interactive web interface at https://mopsmap.net or via download as an offline application. The former is possible as MOPSMAP is computational very efficient. Compared to other data sets with predefined aerosol components, such as OPAC (Hess et al., 1998), compared to existing online Mie tools such as the one provided by Prahl (2018), and compared to GUI tools such as MiePlot Laven (2018), MOPSMAP is more flexible with respect to the characteristics of the aerosol ensembles. Moreover, our data set considers not only spherical particles but also spheroids and a small set of irregularly shaped dust parti-

cles. The output includes ASCII tables for further evaluation, netCDF files for direct application in the radiative transfer model uvspec (Emde et al., 2016), and plots, e.g., for educational purposes.

In Sect. 2, after defining aerosol properties, we describe how existing optical modeling codes were applied (green box in Fig. 1) to create the optical data set of single particles (yellow box). Subsequently, in Sect. 3, we describe the Fortran program (orange box) that uses this data set to calculate optical properties of user-defined particle ensembles. The web interface for online application of the MOPSMAP package is introduced in Sect. 4. To demonstrate the potential of MOPSMAP, several applications are discussed in Sect. 5 before we sum up our paper and give an outlook.

2　Background and the MOPSMAP data set

The optical properties of a particle with known microphysical properties are calculated by optical modeling. For the creation of the basic data set of MOPSMAP, optical modeling of single particles has been performed. In this section, we first define microphysical and optical properties of single particles and then describe how we created the data set using existing optical modeling codes.

We emphasize that the data set is, in principle, applicable to the complete electromagnetic spectrum; however, we use, for simplicity, the term "light" and consequently "optics" instead of more general terms.

2.1　Definition of particle properties

The description of particle properties is well-established and can be found in textbooks with varying levels of detail. Thus, we can restrict ourselves to a brief summary of those properties that are of special relevance for MOPSMAP.

The microphysical properties of an aerosol particle are described by its shape, size, and chemical composition.

Atmospheric aerosols might be spherical in shape but many types consist of nonspherical particles, often

with a large variety of different shapes. Mineral dust (e.g., Kandler et al., 2009) and volcanic ash aerosols (e.g., Schumann et al., 2011b) are important examples of the latter, but, for example, pollen, dry sea salt or soot particles are also usually nonspherical. A quite common approach to consider the particle shape is the approximation using spheroids or distributions of spheroids (Hill et al., 1984; Mishchenko et al., 1997; Kahn et al., 1997; Dubovik et al., 2006; Wiegner et al., 2009). Spheroids originate from the rotation of ellipses about one of their axes. Only one parameter is required for the shape description. Mishchenko and Travis (1998) use the "axial ratio" ϵ_m, which is the ratio between the length of the axis perpendicular to the rotational axis and the length of the rotational axis. By contrast, Dubovik et al. (2006) use the "axis ratio" ϵ_d, defined as the inverse of ϵ_m. Spheroids with $\epsilon_m < 1$, $\epsilon_d > 1$ are called prolate (elongated) whereas spheroids with $\epsilon_m > 1$, $\epsilon_d < 1$ are oblate (flat) spheroids. The aspect ratio ϵ' is the ratio between the longest and the shortest axis, i.e., $\epsilon' = \frac{1}{\epsilon_m} = \epsilon_d$ in the case of prolate spheroids and $\epsilon' = \epsilon_m = \frac{1}{\epsilon_d}$ in the case of oblate spheroids. Spheroids with $\epsilon' = 1$ are spheres.

The size of a particle is commonly described by its radius or diameter. While this is unambiguous in the case of spheres, more detailed specifications are necessary for any kind of nonspherical particles. Often the size of an equivalent sphere is used for the description of the nonspherical particle size: the volume-equivalent radius r_v of a particle with known volume V (containing the particle mass, i.e., without cavities) is

$$r_v = \sqrt[3]{\frac{3V}{4\pi}}, \qquad (1)$$

whereas the cross-section-equivalent radius r_c of a particle with known orientation-averaged geometric cross section C_{geo} is

$$r_c = \sqrt{\frac{C_{geo}}{\pi}}. \qquad (2)$$

In the case of spheroids, r_c is equal to the radius of a sphere having the same surface area (as used by Mishchenko and Travis, 1998). For the conversion between r_v and r_c, the radius conversion factor

$$\xi_{vc} = \frac{r_v}{r_c} = \sqrt[3]{\frac{3\sqrt{\pi}}{4} \frac{V}{C_{geo}^{3/2}}} \qquad (3)$$

is used (Gasteiger et al., 2011b). ξ_{vc} is equal to 1 in the case of spheres and decreases with increasing deviation from a spherical shape. Another definition of size is given by the radius of a sphere that has the same ratio between volume and geometric cross section as the particle

$$r_{vcr} = \frac{3V}{4C_{geo}} = \xi_{vc}^3 r_c. \qquad (4)$$

This definition corresponds to the case "VSEQU" presented by Otto et al. (2011), to the "effective radius" in Eq. (5) of Schumann et al. (2011a), and is more sensitive to non-sphericity than r_v or r_c. For example, a particle with $r_c = 1 \,\mu m$ and $\xi_{vc} = 0.9$ implies that $r_v = 0.9 \,\mu m$ and $r_{vcr} = 0.729 \,\mu m$.

For setting up a data set of optical properties for different wavelengths, it is highly beneficial to make use of the size parameter

$$x = \frac{2\pi r}{\lambda}. \qquad (5)$$

The size parameter x describes the particle size relative to the wavelength λ. The advantage of using x is that optical properties (q_{ext}, ω_0, and $\mathbf{F}$, as defined below) at a given wavelength are fully determined by its shape, refractive index m, and x. Equivalent size parameters x_v, x_c, and x_{vcr} are calculated from the equivalent radii, analogously to Eq. (5).

The chemical composition of a particle determines its complex wavelength-dependent refractive index m. The imaginary part m_i is relevant for the absorption of light inside the particle, whereby an imaginary part of zero corresponds to non-absorbing particles.

The optical properties of a nonspherical particle depend on the orientation of the particle relative to the incident light. In our data set we assume that particles are oriented randomly; thus, the optical properties are stored as orientation averages (Mishchenko and Yurkin, 2017).

The orientation-averaged optical properties at a given wavelength are fully described by the extinction cross section C_{ext}, the single-scattering albedo ω_0 and the scattering matrix $\mathbf{F}(\theta)$, where θ is the angle by which the incoming light is deflected during the scattering process ("scattering angle"). The extinction cross section C_{ext} can be normalized by the orientation-averaged geometric cross section C_{geo} of the particle giving the extinction efficiency

$$q_{ext} = \frac{C_{ext}}{C_{geo}} = \frac{C_{ext}}{\pi r_c^2}. \qquad (6)$$

The single-scattering albedo ω_0 is given by

$$\omega_0 = \frac{C_{sca}}{C_{ext}}, \qquad (7)$$

where C_{sca} is the scattering cross section.

For the scattering matrix $\mathbf{F}$ of randomly oriented particles, we use the notation of Mishchenko and Travis (1998), i.e.,

$$\mathbf{F}(\theta) = \begin{bmatrix} a_1(\theta) & b_1(\theta) & 0 & 0 \\ b_1(\theta) & a_2(\theta) & 0 & 0 \\ 0 & 0 & a_3(\theta) & b_2(\theta) \\ 0 & 0 & -b_2(\theta) & a_4(\theta) \end{bmatrix} \qquad (8)$$

with six independent matrix elements. The scattering matrix describes the transformation of the incoming Stokes vector

I^{inc} to the scattered Stokes vector I^{sca}:

$$I^{\mathrm{sca}}(\theta) = \frac{C_{\mathrm{sca}}}{4\pi R^2} \mathbf{F}(\theta) I^{\mathrm{inc}}, \tag{9}$$

where the Stokes vectors (van de Hulst, 1981) have the shape

$$I = \begin{bmatrix} I \\ Q \\ U \\ V \end{bmatrix} \tag{10}$$

and R is the distance of the observer from the particle. The Stokes vectors I describe the polarization state of light, with the first element I describing its total intensity. Thus, $\mathbf{F}$ is relevant for the polarization of the scattered light, and its first element a_1, which is known as the phase function, is important for the angular intensity distribution of the scattered light. The phase function is normalized such that

$$\int_{0°}^{180°} a_1(\theta) \cdot \sin\theta \cdot \mathrm{d}\theta = 2. \tag{11}$$

For many applications it is useful to expand the elements of the scattering matrix using generalized spherical functions (Hovenier and van der Mee, 1983; Mishchenko et al., 2016). The scattering matrix elements at any scattering angle θ are then determined by a series of θ-independent expansion coefficients α_1^l, α_2^l, α_3^l, α_4^l, β_1^l, and β_2^l, with index l from 0 to $l_{\max}$, see Eqs. (11)–(16) in Mishchenko and Travis (1998). $l_{\max}$ depends on the required numerical accuracy as well as on the scattering matrix itself. For example, in the case of strong forward scattering peaks (typically occurring at large x), $l_{\max}$ needs to be larger than in the case of more flat phase functions, to get the same accuracy.

The asymmetry parameter g is an integral property of the phase function:

$$g = \frac{1}{2} \int_{0°}^{180°} \cos\theta \cdot a_1(\theta) \cdot \sin\theta \cdot \mathrm{d}\theta. \tag{12}$$

g is the average cosine of the scattering angle of the scattered light and is calculated from the expansion coefficients by

$$g = \alpha_1^1 / 3. \tag{13}$$

2.2 Optical modeling of single particles

Depending on the particle type, different approaches are available for calculating particle optical properties. For the creation of the MOPSMAP optical data set, we use the well-known Mie theory (Mie, 1908; Horvath, 2009) in the case of spherical particles, which is a numerically exact approach over a very broad range of sizes. For spheroids we use the T-matrix method (TMM), which is a numerically exact method but limited with respect to maximum particle size. For larger spheroids not covered by TMM, we apply the improved geometric optics method (IGOM). For irregularly shaped particles the discrete dipole approximation (DDA) is applied.

2.2.1 Mie theory

We use the Mie code developed by Mishchenko et al. (2002) for optical modeling of spherical particles. In contrast to the nonspherical particle types described below, we do not store the optical properties of single particles (in a strict sense) because the properties of spheres can be strongly size-dependent, which would require a very high size resolution of our data set (e.g., Chýlek, 1990). Instead, we store data averaged over very narrow size bins, allowing us to use a lower size resolution resulting in a smaller storage footprint of the data set. For each size parameter grid point x, we actually consider a size parameter bin covering the range from $x/\sqrt{1.01}$ to $x \cdot \sqrt{1.01}$ and apply the Mie code for 1000 logarithmically equidistant sizes within that bin before these results are averaged and stored.

2.2.2 T-matrix method (TMM)

We use the extended precision version of the code described by Mishchenko and Travis (1998) for modeling optical properties of spheroids. To improve the coverage of the particle spectrum (x, ϵ_m, and m), internal parameter values of the TMM code, which primarily determine the limits of the convergence procedures, were increased (NPN1 = 290; NPNG1 = 870; NPN4 = 260) as discussed by Mishchenko and Travis (1998). Though, in general, the TMM provides exact solutions for scattering problems, nonphysical results might be obtained due to numerical problems. To reduce the probability of nonphysical results and to increase the accuracy of the results, the parameter DDELT, i.e., the absolute accuracy of computing the expansion coefficients, was set to 10^{-6} (default 10^{-3}). In non-converging cases, which occurred near the upper limit of the covered size range, the requirements were relaxed to DDELT $= 10^{-3}$. Cases that did not converge even with the relaxed DDELT were not included in the data set. Nevertheless, some nonphysical results were obtained by this approach, for example, $\omega_0 > 1$, or outliers of otherwise smooth $\omega_0(x)$ or $g(x)$ curves. Thus, for plausibility checks for each particle shape and refractive index, single-scattering albedos ω_0 and asymmetry parameters g were plotted over size parameter x and outliers were recalculated with slightly modified size parameters. Recalculations with nonphysical results were not included in the data set, which reduces the upper limit of the covered size range for that particular particle shape and refractive index.

2.2.3 Improved geometric optics method (IGOM)

Optical properties of large spheroids were calculated with the improved geometric optics method (IGOM) code provided by Yang et al. (2007) and Bi et al. (2009). In general, this approximation is most accurate if the particle and its structures are large compared to the wavelength. In addition to reflection, refraction, and diffraction by the particle, which

are considered by classical geometric optics codes, IGOM also considers the so-called edge effect contribution to the extinction efficiency q_{ext} (Bi et al., 2009). Classical geometric optics results in $q_{ext} = 2$, whereas q_{ext} is variable in the case of IGOM. The default settings of the code were used. The minimum size parameter was selected depending on the maximum size calculated with TMM.

2.2.4 Discrete dipole approximation code ADDA

Natural nonspherical aerosol particles, such as desert dust particles, comprise practically an infinite number of particle shapes; thus, it is impossible to cover the full range of shapes in aerosol models. Moreover, the shape of each individual particle is never known under realistic atmospheric conditions. Consequently, typical irregularities such as flat surfaces, deformations or aggregation of particles can be considered only in an approximating way. To enable the user of MOPSMAP to investigate the effects of such irregularities the properties of six exemplary irregular particle shapes, as introduced by Gasteiger et al. (2011b), are provided. The geometric shapes were constructed using the object modeling language Hyperfun (Valery et al., 1999). The first three shapes are prolate spheroids with varying aspect ratios (A: $\epsilon' = 1.4$; B: $\epsilon' = 1.8$; C: $\epsilon' = 2.4$) and surface deformations according to Gardner (1984). Shape D is an aggregate composed of 10 overlapping oblate and prolate spheroids; surface deformations were applied as for shapes A–C. Shape E and F are edged particles with flat surfaces and a varying aspect ratio.

The optical properties were calculated with the discrete dipole approximation code ADDA (Yurkin and Hoekstra, 2011). A large number of particle orientations needs to be considered for the determination of orientation-averaged properties. ADDA provides an optional built-in orientation averaging scheme in which the calculations for the required number of orientations is done within a single run. An individual ADDA run using this scheme requires approximately the time for one orientation multiplied with the number of orientations (typically a few hundred), which can result in computation times of several weeks for large x. Because of the long computation times we split them up and performed independent ADDA runs for each orientation. The orientation-averaged properties are calculated in a subsequent step using the ADDA results for the individual orientations (see below).

The computational demand of DDA calculations increases strongly with size parameter x, typically with about x^5 to x^6. Thus, when aiming for large x, which is required for mineral dust in the visible wavelength range, it is necessary to find code parameters and an orientation averaging approach that provide a compromise between computation speed and accuracy.

The ADDA code mainly allows the following code parameters to be optimized:

– DDA formulation

– stopping criterion of the iterative solver

– number of dipoles per wavelength.

We estimate the accuracy of the ADDA results by comparing orientation-averaged q_{ext}, q_{sca}, $a_1(0°)$, $a_1(180°)$, and $a_2(180°)/a_1(180°)$ with results obtained using more strict calculation parameters. Accuracy tests are performed for shapes B and C, for size parameters $x_v = 10.0$, 12.0, 14.4, 17.3, 19.0, and 20.8, and for refractive index $m = 1.52 + 0.0043i$; i.e., 12 single particle cases are considered in total. By comparing the different DDA formulations available in ADDA, it was found that the filtered coupled-dipole technique (ADDA command line parameter "-pol fcd -int fcd"), as introduced by Piller and Martin (1998) and applied by Yurkin et al. (2010), offers the best compromise between computation speed and accuracy of modeled optical properties. Using a stopping criterion for the iterative solver of 10^{-4} instead of 10^{-3} only has negligible influence on optical properties ($< 0.1\%$) but requires approximately 30 % more computation time; thus, we used 10^{-3} for the ADDA calculations to create our data set. The extinction efficiency q_{ext} and the scattering efficiency q_{sca} change in all cases by less than 0.3 % if a grid density of 16 dipoles per wavelength is used instead of 11. The maximum relative changes due to the change in dipole density are 0.2 % for $a_1(0°)$, 1.7 % for $a_1(180°)$, and 1.9 % for $a_2(180°)/a_1(180°)$. Because of the large difference in computation time, which is about a factor of 3–4, and the low loss in accuracy, about 11 dipoles per wavelength were selected for the MOPSMAP data set. For $x_v < 10$ we use the same dipole set as for $x_v = 10$ so that the number of dipoles per wavelength increases with decreasing x_v, being about $110/x_v$.

The particle orientation is specified by three Euler angles (α_e, β_e, γ_e) as described by Yurkin and Hoekstra (2011) and basically a step size of 15° is applied for β_e and γ_e resulting in 206 independent ADDA runs for each irregular particle. The orientation sampling and averaging is described in detail in Sect. S1.1 of the Supplement.

To test the accuracy of the selected orientation averaging scheme, orientation-averaged optical properties for shapes B, C, D, and F were compared to results using a much smaller step of 5° for β_e and γ_e. These calculations consider about 12 times more orientations than the calculations used for MOPSMAP. Details are presented in Sect. S1.2 of the Supplement. Maximum deviations of less than 1 % are found for q_{ext}, q_{sca}, and $a_1(0°)$. For backscatter properties, $a_1(180°)$ and $a_2(180°)/a_1(180°)$, typical deviations are of the order of a few percent (max. 14 %). Moreover, in Sect. S1.3 of the Supplement, the selected orientation averaging scheme is applied to spheroids, and their optical properties are compared to reference TMM results. These deviations are comparable to those given in Sect. S1.2.

Table 1. Microphysics of spheres and spheroids considered in the MOPSMAP data set.

Method	Mie	TMM	IGOM
Particle shape	spheres	oblate and prolate spheroids $\epsilon' = 1.2, 1.4, ..., 3.0, 3.4, 3.8, ..., 5.0$	
Size parameter	$10^{-6} < x_c < 1005$ $\frac{x_{i+1}}{x_i} = 1.01$ size bins	$10^{-6} < x_c < (5 - 125)$ $\frac{x_{i+1}}{x_i} = 1.05$ single size	$(5 - 125) < x_c < 1005$ $\frac{x_{i+1}}{x_i} = 1.10$ single size
m_r	$(0.1, 0.2, ..., 0.9, 1.0)^*, 1.04, 1.08, ..., 1.68, 1.76, ..., 2.0, 2.2, ..., 3.0$		
m_i	0, 0.0005375, 0.001075, 0.0015203, 0.00215, 0.0030406, 0.0043, 0.0060811, 0.0086, 0.0121622, 0.0172, 0.0243245, 0.0344, 0.0486490, 0.0688, 0.0972979, 0.1376, 0.2752, 0.5504, 1.1008, 2.2016		

* IGOM was not applied to $m \leq 1.0$.

Table 2. Microphysics of irregularly shaped particles considered in the MOPSMAP data set.

Particle shape	Shapes A–F, Fig. 1 of Gasteiger et al. (2011b)
Size parameter	$10^{-3} < x_v < 30.2; \frac{x_{i+1}}{x_i} \approx 1.10$; single size
m_r	1.48, 1.52, 1.56, 1.60
m_i	0, 0.00215, 0.0043, 0.0086, 0.0172, 0.0344, 0.0688

In summary, ADDA with the filtered coupled-dipole technique, at least 11 dipoles per wavelength and a stopping criterion for the iterative solver of 10^{-3} was used for optical modeling of the irregularly shaped particles in our data set together with the orientation averaging scheme combining 206 ADDA runs. Tests demonstrate that the modeling accuracy is mainly determined by the applied orientation averaging scheme.

2.3 Optical data set

Using the codes with the settings described above, a data set of modeled optical properties of single particles in random orientation was created. For spheres, we stored averages over narrow size bins as described above instead of single particle properties. An overview over the wide range of sizes, shapes, and refractive indices of the particles in the data set is given in Tables 1 and 2. For each combination of refractive index and shape a separate netCDF file was created, e.g., "spheroid_0.500_1.5200_0.008600.nc" for spheroids with $\epsilon_m = 0.5$ (prolate with $\epsilon' = 2.0$) and $m = 1.52 + 0.0086i$. Each file contains the optical properties on a grid of size parameters. The complete data set requires about 42 gigabytes of storage capacity.

For spheres and spheroids the minimum size parameter is set to 10^{-6}, and the maximum size parameter is set to $x \approx 1005$ to cover, e.g., $r_c = 80 \, \mu m$ at $\lambda = 500 \, nm$. The size increment is 1 % (i.e., $x_{i+1}/x_i = 1.01$) in the case of spheres, 5 % in the case of TMM spheroids, and 10 % for IGOM spheroids. In the case of spheroids having refractive indices most relevant for atmospheric studies, the TMM is applied up to (or close to) the largest possible size parameter with the approach described in Sect. 2.2.2. The maximum size parameter of the TMM calculations is reduced for less relevant refractive indices. An overview is given in Sect. S2 of the Supplement and a detailed list of the maximum size parameters for all m and ϵ_m combinations can be downloaded from Gasteiger and Wiegner (2018). The maximum size parameter for TMM is in the range $5 < x < 125$, strongly depending on m and particle shape, and determines the lowest size parameter at which IGOM may be applied. The first IGOM size parameter is between 0 and 10 % larger than the maximum TMM size parameter. The TMM and IGOM results for spheroids are merged into a single netCDF file covering the complete size range from $x = 10^{-6}$ to $x \approx 1005$, which is sufficient for most applications. For example, for prolate spheroids with $\epsilon' = 1.8$ and $m = 1.56 + 0i$, the size range from $x = 10^{-6}$ to $x = 88.22$ is covered by TMM; IGOM starts at $x = 89.54$. The transition from TMM to IGOM for several scattering angles is demonstrated in Sect. S3 of the Supplement. Since IGOM is an approximation, unrealistic jumps of optical properties may occur at the transition. For typical mineral dust ensembles in the visible spectrum, particles in the IGOM range contribute less than 10 % to the total extinction. IGOM was not applied to $m_r < 1.04$; thus, the size parameter range is limited to the TMM range for these refractive indices. A step of 0.04 was selected for the m_r grid in the most relevant range (from 1.00 to 1.68) and a wider m_r step elsewhere. The development of the data set started with $m_i = 0.0043$, and beginning from this value, m_i was increased and decreased in steps of a factor $\sqrt{2}$. Below $m_i = 0.001$ and above $m_i = 0.1$, the step width is a factor 2.

The optical data for the irregularly shaped particles (Table 2) are limited to $x_v \leq 30.2$ because of the huge computation requirements for optical modeling of large particles. Nonetheless, the most important range for many applications is covered; e.g., at $\lambda = 1064$ nm particles up to $r_v = 5.1$ μm can be modeled. The m grid for the irregularly shaped particles is limited to the most relevant range for desert dust in the visible spectrum, and the m_i step is set to a factor of 2. The quantification of the conversion factor ξ_{vc} of the six irregular shapes requires the determination of their orientation-averaged geometric cross sections, which is done numerically.

The optical properties stored for each particle are the extinction efficiency q_{ext}, the scattering efficiency q_{sca}, and the expansion coefficients α_1^l, α_2^l, α_3^l, α_4^l, β_1^l, and β_2^l of the scattering matrix. The ADDA and the IGOM code provide the angular-resolved scattering matrix elements, which we converted to the expansion coefficients stored in the data set following the method described by Hovenier and van der Mee (1983) and Mishchenko et al. (2016). We optimized the expansion coefficients for accurate scattering matrices at 180°, which is probably the most error sensitive angle. As a byproduct, lidar applications will certainly benefit from this optimization.

In the case of asymmetric shapes in random orientation, the scattering matrix has 10 independent elements as discussed by van de Hulst (1981). By using only six elements of **F** (Eq. 8) in our data set, we implicitly assume that each irregular model particle (shapes A–F) occurs as often as its mirror particle, which is formed by mirroring at a plane (van de Hulst, 1981).

Figure 2 shows an example from the MOPSMAP optical data set. The refractive index is set to $m = 1.56 + 0.00215i$, which is representative of desert dust particles at visible wavelengths. The properties of spherical particles are shown in blue, whereas the properties of prolate spheroids with $\epsilon' = 1.4$ and 3.0 are shown in orange and green, respectively. Red and violet lines denote irregularly shaped particles D and F, respectively. Figure 2a shows the extinction efficiency q_{ext} as a function of cross-section-equivalent size parameter x_c. The general shape of the $q_{ext}(x_c)$ curve is similar for the different shapes; nonetheless, with increasing deviation from a spherical shape, the amplitudes of the oscillations of $q_{ext}(x_c)$ become smaller and a shift in the maximum q_{ext} towards larger x_c is found. Figure 2b shows the single-scattering albedo ω_0 for the same particles as Fig. 2a. For particle sizes comparable to the wavelength, ω_0 reaches maxima with values of about 0.991, almost independent of particle shape. ω_0 approaches a value of about 0.551 at $x_c \approx 1000$ for spheres and spheroids. Fig. 2c shows the asymmetry parameter g. When the particle size becomes comparable to the wavelength, g increases and oscillates as a function of x_c, with the strongest oscillations occurring in the case of spheres. There is some shape dependence of g for $x_c > 5$; in particular, the aggregate shape results in systematically smaller g than the other
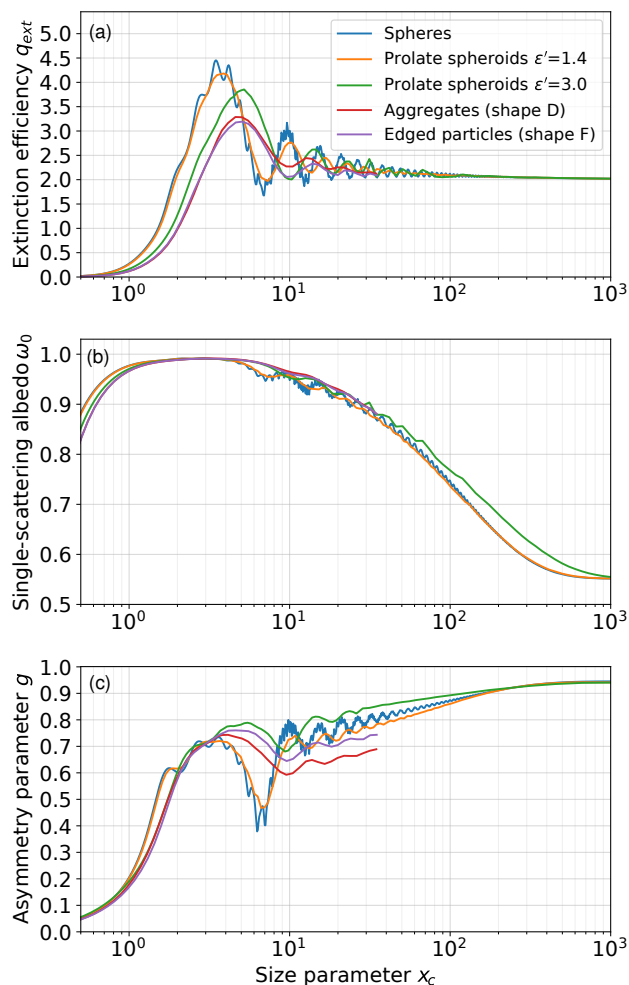

Figure 2. Optical properties of single particles (or narrow size bins in the case of spheres) with fixed refractive index $m = 1.56 + 0.00215i$ as a function of size parameter. The different colors denote different particle shapes. Panel **(a)** shows the extinction efficiency q_{ext}, panel **(b)** the single-scattering albedo ω_0, and panel **(c)** the asymmetry parameter g.

shapes for $x_c > 10$. The transition from the numerically exact TMM to the IGOM approximation occurs at $x_c \approx 125$ for $\epsilon' = 1.4$ (orange line) and at $x_c \approx 27$ for $\epsilon' = 3.0$ (green line) and is quite smooth.

3 MOPSMAP Fortran program

In this section the basic characteristics of the MOPSMAP Fortran program to calculate optical properties of particle ensembles are described. Besides a modern Fortran compiler, e.g., gfortran 6 or above, the netCDF Fortran development source code is required to build the executable. The computation time and memory requirements depend on the ensemble complexity and the number of wavelengths but in general are
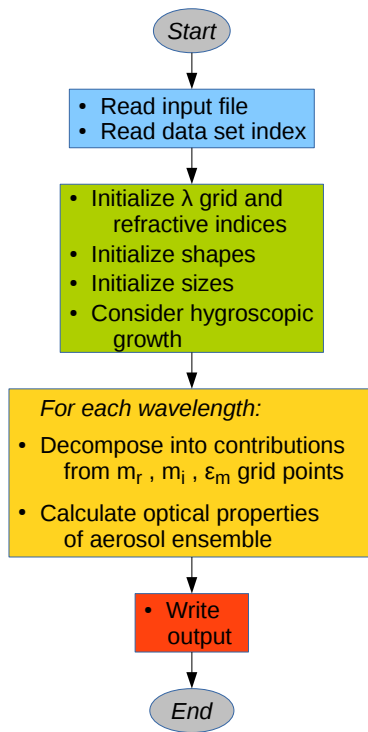
Figure 3. Simplified flow chart of the MOPSMAP Fortran program.

low for state-of-the-art personal computers. The Fortran code and the data set are available for download from Gasteiger and Wiegner (2018), and a web interface (see Sect. 4) provides online access to most of the functionality of the Fortran program without the requirement of downloading the code and the data set.

Within each MOPSMAP run the optical properties of a specific user-defined ensemble are calculated at a user-defined wavelength grid. The ensemble microphysics and the wavelength grid are defined in an input file. The details about the options available for the input file are described in a user manual which is provided together with the code.

Figure 3 shows a flow chart of the MOPSMAP Fortran program. The program is initialized by reading the input file and a data set index. The latter contains information on the refractive index and shape grid and the size parameter ranges covered by the data set. Then, all information required for the optical modeling is initialized, for example the set of wavelengths, the refractive indices as a function of wavelength, shape distributions, and the effect of the hygroscopic growth, before the optical calculations are performed for each wavelength, as described in the following.

3.1 Calculation of optical properties of particle ensembles

Usually aerosol particles occur as ensembles of particles of different size, refractive index, and/or shape. The different particles contribute to the optical properties of the ensemble. Assuming that the distance between the particles is large enough for interaction of light with each particle to occur without influence from any other particle ("independent scattering"; van de Hulst, 1981), the contribution of each particle can be added as described below.

In MOPSMAP particle ensembles are composed of one or more independent modes (the terms "mode" and "component" are often used synonymously in the literature). Each mode in MOPSMAP is characterized by particle size, shape, and refractive index, whereby each property can be described as a fixed value or as a distribution (see below). As these parameters do not necessarily correspond to the grid points of the MOPSMAP data set, for each mode (and each wavelength), decomposition into contributions from the different available m and shapes of the data set needs to be performed.

For a mode containing spheroids, in the most simple but probably most frequently used case of fixed values of m_r, m_i, and ϵ_m, linear interpolation in the three-dimensional (m_r, m_i, ϵ_m) space of the MOPSMAP data set is performed; i.e., eight grid points contribute to the result, with each grid point weighted according to the normalized distance from the parameters of the mode. For each dimension, the contributing grid points are the nearest grid point smaller or larger than the value of the mode; e.g., for the real part of the refractive index m_r

$$m_{r,i} \leq m_r < m_{r,i+1}. \tag{14}$$

The weight of the grid points $m_{r,i}$ and $m_{r,i+1}$ is

$$w_{m_r,i} = \frac{m_{r,i+1} - m_r}{m_{r,i+1} - m_{r,i}}, \tag{15}$$

$$w_{m_r,i+1} = \frac{m_r - m_{r,i}}{m_{r,i+1} - m_{r,i}}. \tag{16}$$

Finally the weights for each of the eight contributions are calculated as the products of the weights determined for each dimension. An example is shown in Sect. S4 of the Supplement. The error in the interpolation of the user-specified values between the grid points of the data set is discussed in Sect. 3.3

Under other conditions more or less than eight contributions have to be considered. In the case of spheres or a single irregular shape, an interpolation in the shape dimension is not necessary, so that four contributions are sufficient. In the case of a spheroid aspect ratio distribution, contributions from all required ϵ_m grid points are considered and weighted according to the given distribution. In the case of a mode containing a non-absorbing fraction (see below), an additional m_i grid point, $m_i = 0$, may be required. Furthermore,

because of the limited size range of irregularly shaped particles in the data set, a special treatment can be applied: a MOPSMAP option is available which substitutes irregularly shaped particles above a selected size parameter with other particle shapes, spherical or nonspherical, as selected by the user. As a consequence, the particle shape of that mode becomes size- and wavelength-dependent and the number of different contributions increases. The total number of contributions for an ensemble, denoted as J in the following, varies because the number of modes is not fixed and, as just discussed, the number of contributions from each mode depends on the characteristics of each mode. This underlines the flexibility of MOPSMAP.

The optical properties of the particle ensemble are calculated for each wavelength by summation over extensive properties of all particles described by the J contributions. This approach corresponds to the so-called external mixing of particles. Each contribution has a size distribution $n_j(r)$, i.e., a particle number concentration per particle radius interval from r to $r + dr$, in the range from $r_{\min,j}$ to $r_{\max,j}$, which is obtained by multiplying the user-defined size distribution of the mode with the weights obtained during the decomposition. The extinction coefficient α_{ext} and the scattering coefficient α_{sca} are calculated by

$$\alpha_{\mathrm{ext}} = \sum_{j=1}^{J} \left(\int_{r_{\min,j}}^{r_{\max,j}} C_{\mathrm{ext},j}(r) \cdot n_j(r) \cdot dr \right), \quad (17)$$

$$\alpha_{\mathrm{sca}} = \sum_{j=1}^{J} \left(\int_{r_{\min,j}}^{r_{\max,j}} C_{\mathrm{sca},j}(r) \cdot n_j(r) \cdot dr \right). \quad (18)$$

The expansion coefficients need to be weighted with $C_{\mathrm{sca},j}(r)$; for example, α_1^l of a particle ensemble is calculated by

$$\alpha_1^l = \frac{1}{\alpha_{\mathrm{sca}}} \cdot \sum_{j=1}^{J} \left(\int_{r_{\min,j}}^{r_{\max,j}} \alpha_{1,j}^l(r) \cdot C_{\mathrm{sca},j}(r) \cdot n_j(r) \cdot dr \right). \quad (19)$$

For the integration of extensive properties over the size distribution, we apply the trapezoidal rule, which assumes linearity between the r grid points.

The size distribution $n(r) = \frac{dN}{dr}$ for each mode can be specified in various ways. The MOPSMAP user can either specify a single size, apply size distribution tables in ASCII format, or apply a size distribution parameterization. The following parameterizations are available:

1. $n(r) = \frac{1}{\sqrt{2\pi} \ln \sigma} \frac{1}{r} \exp\left[-\frac{1}{2} \left(\frac{\ln r - \ln r_{\mathrm{mod}}}{\ln \sigma} \right)^2 \right]$ – lognormal distribution;

2. $n(r) = A r^\alpha \exp(-B r^\gamma)$ – modified gamma distribution, Deirmendjian (1964);

3. $n(r) = A \exp(-Br)$ – exponential distribution, $\alpha = 0$, $\gamma = 1$;

4. $n(r) = A r^\alpha$ – power law distribution, Junge distribution, $B = 0$, Deirmendjian (1964);

5. $n(r) = A r^\alpha \exp(-Br)$ – gamma distribution, $\gamma = 1$, Twomey (1977).

r_{mod} is the mode radius, σ a dimensionless parameter for the relative width of the distribution, and N_0 the total number density (in the range from $r_{\min} = 0$ to $r_{\max} = \infty$) of the lognormal distribution. For the subsequent size distributions, parameters A, α, B, and γ are positive and A controls the scaling of total number density whereas α, B, and γ are relevant for the shape of the size distributions. The exponential distribution, power law distribution, and the gamma distribution are a subset of the modified gamma distribution with the specific parameter values as given above (see also Petty and Huang, 2011).

The particle shape can be specified independently for each mode and is, within each mode, independent of size and refractive index. In the case of spheroids, either a fixed aspect ratio ϵ' or an aspect ratio distribution is used. The latter can be given as a table in an ASCII file or it can be parameterized by a modified lognormal distribution (Kandler et al., 2007)

$$n(\epsilon') = \frac{dN}{N_0 \cdot d\epsilon'} = \quad (20)$$

$$\frac{1}{\sqrt{2\pi} \sigma_{ar} (\epsilon' - 1)} \exp\left[-\frac{1}{2} \left(\frac{\ln(\epsilon' - 1) - \ln(\epsilon'_0 - 1)}{\sigma_{ar}} \right)^2 \right]$$

with parameters ϵ'_0 for the location of the maximum of $n(\epsilon')$ and σ_{ar} for the width of the distribution.

The refractive index of each mode can either be wavelength-independent or specified as a function of wavelength in an ASCII file. In addition, it is possible to specify for each mode a non-absorbing fraction $\mathcal{X}$. If $\mathcal{X} > 0$, the mode is divided, for all sizes and shapes, into a non-absorbing ($m_{i,1} = 0$, relative abundance $\mathcal{X}$) and an absorbing fraction ($m_{i,2} = m_i/(1 - \mathcal{X})$, relative abundance $1 - \mathcal{X}$). As a consequence, the average m_i over all particles of the mode remains equal to the m_i as specified by the user. This non-absorbing fraction approach can be used as a parameterization of the refractive index variability within desert dust ensembles as described by Gasteiger et al. (2011b) and below in Sect. 5.6.

For the hygroscopic particle growth the following parameterization (Petters and Kreidenweis, 2007; Zieger et al., 2013)

$$\frac{r_{\mathrm{wet}}(\mathrm{RH})}{r_{\mathrm{dry}}} = \left(1 + \kappa \cdot \frac{\mathrm{RH}}{1 - \mathrm{RH}} \right)^{\frac{1}{3}} \quad (21)$$

is implemented in MOPSMAP, where RH is the relative humidity and κ the hygroscopic growth parameter of the particles of each mode. This equation describes the ratio between

the size of the particle at a given RH and the size of the particle in a dry environment (RH = 0 %). The parameterization implies that this ratio is independent of size; thus, for example in the case of a lognormal size distribution, r_{min}, r_{max}, and r_{mod} are multiplied with this ratio, whereas the relative width σ of the distribution is not modified. This is the usual approach though modal representations of aerosol size distributions may also predict higher moments (Binkowski and Shankar, 1995; Zhang et al., 2002), and thus σ can be a prognostic variable as well. The refractive index is modified by the water taken up following the volume weighting rule. Both RH and κ can be chosen by the user. This parameterization is valid for particles with $r > 40$ nm, where the Kelvin effect can be neglected (Zieger et al., 2013). It is worth noting that this parameterization differs from the relative humidity dependence implemented in OPAC, which was adapted from Hänel and Zankl (1979).

3.2 Output of Fortran program

As output of MOPSMAP the following properties of aerosol ensemble are available. Redundant properties, such as lidar-related properties, are available to facilitate the use of the results:

- extinction coefficient α_{ext} (m^{-1})

- single-scattering albedo ω_0

- asymmetry parameter g

- effective radius $r_{eff} = \frac{\int r^3 n(r) \mathrm{d}r}{\int r^2 n(r) \mathrm{d}r}$ (μm) (referring to r_c, r_v, or r_{vcr} as selected by the user)

- number density N (m^{-3}) (number of particles per atmospheric volume)

- cross section density a (m^{-1}) (particle cross section per atmospheric volume)

- volume density v (particle volume per atmospheric volume)

- mass concentration M (gm^{-3}) (particle mass per atmospheric volume)

- expansion coefficients (α_1^l to β_2^l) for elements of scattering matrix

- scattering matrix elements (a_1 to b_2) at user defined angle grid

- volume scattering function $\widetilde{a}_1 = \frac{\alpha_{ext} \cdot \omega_0}{4\pi} \cdot a_1$ (m^{-1} sr^{-1}) at user defined angle grid

- backscatter coefficient $\beta = \frac{\alpha_{ext} \cdot \omega_0}{4\pi} \cdot a_1(180°)$ (m^{-1} sr^{-1})

- lidar ratio $S = \frac{4\pi}{\omega_0 a_1(180°)}$ (sr)

- linear depolarization ratio $\delta_l = \frac{a_1(180°) - a_2(180°)}{a_1(180°) + a_2(180°)}$

- Ångström exponents $\mathrm{AE}_\zeta = -\frac{\log \frac{\zeta(\lambda_1)}{\zeta(\lambda_2)}}{\log \frac{\lambda_1}{\lambda_2}}$ for $\zeta \in \{\alpha_{ext}, \alpha_{sca}, \alpha_{abs}, \beta\}$

- extinction-to-mass conversion factor $\eta = \frac{M}{\alpha_{ext}}$ (g m^{-2})

- mass-to-backscatter conversion factor $Z = \frac{\beta}{M}$ (m^2 sr^{-1} g^{-1}).

Scattering matrix elements and the quantities derived from them are calculated from the expansion coefficients. Wavelength-independent properties r_{eff}, N, a, v, and M are calculated for each wavelength to demonstrate the numerical accuracy of the integration.

The results are available in ASCII and in netCDF format. The format of the program output is described in the user manual. The netCDF output files can be read by the radiative transfer model uvspec, which is included in libRadtran (Mayer and Kylling, 2005; Emde et al., 2016).

3.3 Interpolation and sampling error

Due to the limited size resolution in the data set and required interpolations between refractive index and aspect ratio grid points, deviations from exact model calculations for specific microphysical properties occur. As examples, Fig. 4 illustrates deviations introduced for single particle properties, whereas Table 3 shows deviations for particle ensembles.

In Fig. 4a and c effects of the limited size resolution on the extinction efficiency q_{ext} and the asymmetry parameter g are shown for non-absorbing spheres and spheroids with $m = 1.52 + 0i$. In particular for spheres with $x > 10$, deviations for single particles can be considerable because of small-scale features that are not resolved in the data set. In the case of spheres these features are implicitly considered in the data set by storing the average over 1000 sizes within each size bin as described above. In the case of spheroids, the data set contains properties calculated for single sizes which may not be fully representative of close-by sizes. However, since the small-scale features are much weaker for spheroids than for spheres, the average deviation for spheroids is much smaller than for spheres.

In Fig. 4b and d effects due to the required interpolation between the refractive index grid points are illustrated for spheres with $m = 1.54 + 0.005i$. While the red lines show the properties calculated from the data set, the black lines show Mie calculations done explicitly for $m = 1.54 + 0.005i$ with the same size grid as used in the data set. The comparison illustrates that MOPSMAP calculates optical properties on average correctly, but some smaller-scale features are lost: for example, the extinction efficiency $q_{ext}(x)$ in the size parameter range from 20 to 40 is dampened compared to the
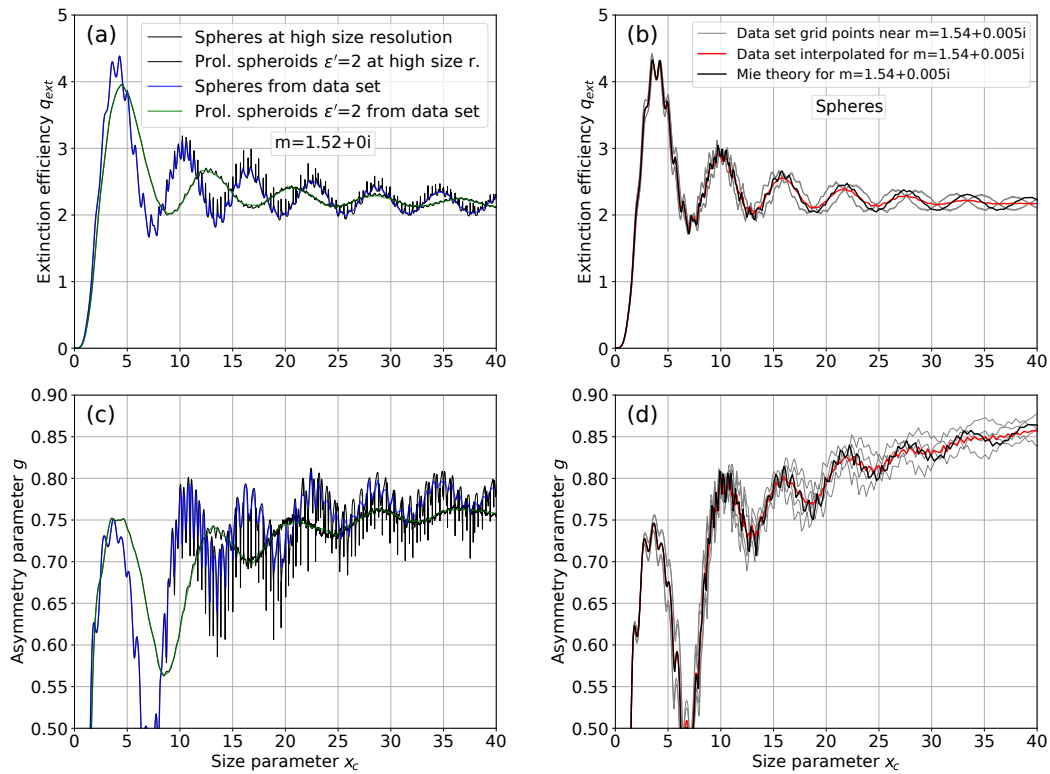
Figure 4. Examples illustrating the effect of the limited size resolution of the MOPSMAP data set **(a, c)** and the effect of the interpolation between the refractive index grid points of the data set **(b, d)**; extinction efficiencies q_{ext} **(a, b)** and asymmetry parameters g **(c, d)** as functions of the size parameter from $x = 0$ to $x = 40$ are compared; in **(a)** and **(c)** the high size-resolution calculations (black lines) were performed with linear x steps of 0.002 in the case of spheres and 0.01 in the case of spheroids; in **(b)** and **(d)** the red lines show properties calculated with MOPSMAP for $m = 1.54 + 0.005i$ by interpolation between refractive indices included in the data set (i.e., between $m = 1.52 + 0.0043i$, $m = 1.52 + 0.0060811i$, $m = 1.56 + 0.0043i$, and $m = 1.56 + 0.0060811i$, for which the properties are shown as thin gray lines), and for comparison, the black lines show the properties calculated by Mie theory explicitly for $m = 1.54 + 0.005i$ using the same x grid as used by the data set.

Table 3. Optical properties calculated for a lognormal mode with $r_{mod} = 0.5\,\mu m$, $\sigma = 2.0$, $r_{min} = 0.001\,\mu m$, and $r_{max} = 4\,\mu m$ at $\lambda = 628.32$ nm. Two cases of particle shapes are considered: spheres and prolate spheroids with $\epsilon' = 2.0$. The columns "data set" contain values calculated using MOPSMAP with the data set described in Sect. 2.3. For comparison, the same properties are calculated in the columns "highres" using a high size resolution and in the columns "explicit" using Mie theory or TMM explicitly at $m = 1.54 + 0.005i$.

	Size sampling example for $m = 1.52 + 0i$				m-interpolation example for $m = 1.54 + 0.005i$			
	Spheres		Spheroids		Spheres		Spheroids	
	Data set	Highres	Data set	Highres	Data set	Explicit	Data set	Explicit
α_{ext} (km^{-1})	4.808	4.808	4.863	4.861	4.793	4.793	4.844	4.846
ω_0	1.0000	1.0000	1.0000	1.0000	0.8845	0.8840	0.8892	0.8886
g	0.7045	0.7045	0.7018	0.7021	0.7331	0.7332	0.7382	0.7380
S (sr)	10.52	10.52	42.75	42.30	13.13	13.36	58.25	58.78
δ_l	0.0000	0.0000	0.3063	0.2986	0.0000	0.0000	0.2502	0.2502

Mie calculation for $m = 1.54 + 0.005i$ because of the interference of the $q_{\text{ext}}(x)$ curves for $m_r = 1.52$ and $m_r = 1.56$ (see gray lines in Fig. 4b; note that curves for different m_i lie almost on top of each other).

For other size ranges, refractive indices, and optical quantities, the effects on the single particle properties are in principle similar but they may vary in magnitude.

Table 3 investigates the sampling and interpolation errors for a mono-modal lognormal size distribution with a typical width of $\sigma = 2.0$. The effective radius is $r_{\text{eff}} = 1.44\,\mu\text{m}$, which is a typical value for transported desert aerosol. Sizes up to $r_{\text{max}} = 4\,\mu\text{m}$, which corresponds to size parameter $x_c = 40$ at $\lambda = 628.32\,\text{nm}$, are considered. The left half of Table 3 compares optical properties calculated from the MOPSMAP data set (columns "data set") with properties calculated using a high size resolution (columns "highres"), the same resolutions as displayed in Fig. 4a. For spheres, the results are equal up to at least the fourth digit. In the case of prolate spheroids with $\epsilon' = 2.0$, deviations are found for the fourth digit of α_{ext} and g. For the lidar-related quantities S and δ_l, the differences are larger with the relative deviation of δ_l being 2.6 %. These differences are caused by the high sensitivity of lidar-related quantities, and it is expected that deviations become smaller when shape distributions or wider size distributions are applied.

The right half of Table 3 demonstrates the effect of the m interpolation for an exemplary $m = 1.54 + 0.005i$. MOPSMAP calculations (columns "data set") are compared to results obtained using explicitly this refractive index in the Mie and TMM calculations. While the effect of the m interpolation is very small for α_{ext}, g, and δ_l, it is slightly larger for ω_0 and S. The maximum relative effect is found for the lidar ratio S of spheres with a deviation of 1.7 %.

These comparisons demonstrate that deviations found for single particles are largely smoothed out in the case of particle ensembles due to the averaging over a large number of different particles. Only for a few special atmospheric applications, for example, the modeling of a rainbow, the limited resolution of the data set may still lead to a considerable error.

4 MOPSMAP web interface

A web interface is provided as part of MOPSMAP at https://mopsmap.net. It was designed to be intuitive for expert and nonexpert users, e.g., for the demonstration of sensitivities of optical properties on microphysical properties in the framework of lectures, but also for a lot of scientific problems as outlined in the following section. The web interface is written in PHP and uses the SQLite library. After the registration as a user, online calculations of optical properties of a large range of particle ensembles can be performed. Input and output can be defined by the user; for nonexpert users, a lot of default ensembles representative of specific climatological conditions are already available. The input parameters primarily include the microphysical properties of the particles. The particles' microphysics are described by up to four components (each described by an individual lognormal size distribution), the wavelength dependence of the refractive index and the shape. Any lognormal size distribution can be used; to facilitate the usage (e.g., for nonexpert users), the aerosol components from the OPAC data set (Hess et al., 1998), e.g., "mineral coarse mode", "water-soluble", or "soot", are already included. The same is true for the 10 "aerosol types" defined in OPAC, e.g., "continental clean", "urban" or "maritime polluted", consisting of a combination of components. Calculations can be made for a single wavelength, for wavelength ranges or a prescribed wavelength set (e.g., for a typical aerosol lidar or a AERONET sun photometer). Moreover, users can define their own wavelength sets, e.g., for a specific radiometer. The relative humidity is selected by the user and it is effective for all hygroscopic components according to Eq. (21). The hygroscopic growth of the OPAC components in MOPSMAP differs from the original OPAC version (Hess et al., 1998); it follows the κ parameterization with the values proposed by Zieger et al. (2013). In the "expert user mode" the flexibility is further increased: the number of components can be larger than four, and the size distribution can be given as discrete values on a user-defined size grid.

The output comprises the complete set of optical properties as described in Sect. 3.2. It can be downloaded for further applications and includes ASCII tables as well as a netCDF file that can be used for radiative transfer calculations with uvspec of the widely used libRadtran package (Emde et al., 2016). To provide an immediate overview over the results, the most important parameters, such as extinction coefficient (α_{ext}), single-scattering albedo (ω_0), asymmetry parameter (g), Ångström exponent (AE), or lidar ratio (S), are displayed as tables when the calculations have been completed. In addition plots of the results as a function of wavelength and scattering angle are shown as selected by the user.

All results are stored in the user's personal folder so that all calculations can be reproduced. Furthermore, all calculations can also easily be rerun with a slightly modified input parameter set.

5 Applications

In this section a selection of examples is presented to demonstrate the wide range of applications of MOPSMAP. Many of them can be performed by using the web interface. Some examples need a local version of MOPSMAP alongside with scripts that repeatedly call the Fortran program. These scripts are written in Python and can be downloaded from Gasteiger and Wiegner (2018) as part of the MOPSMAP package.

It is worth mentioning that numerous studies demonstrate the need for optical modeling of aerosol ensembles, thus illustrating the range of possible applications of MOPSMAP.
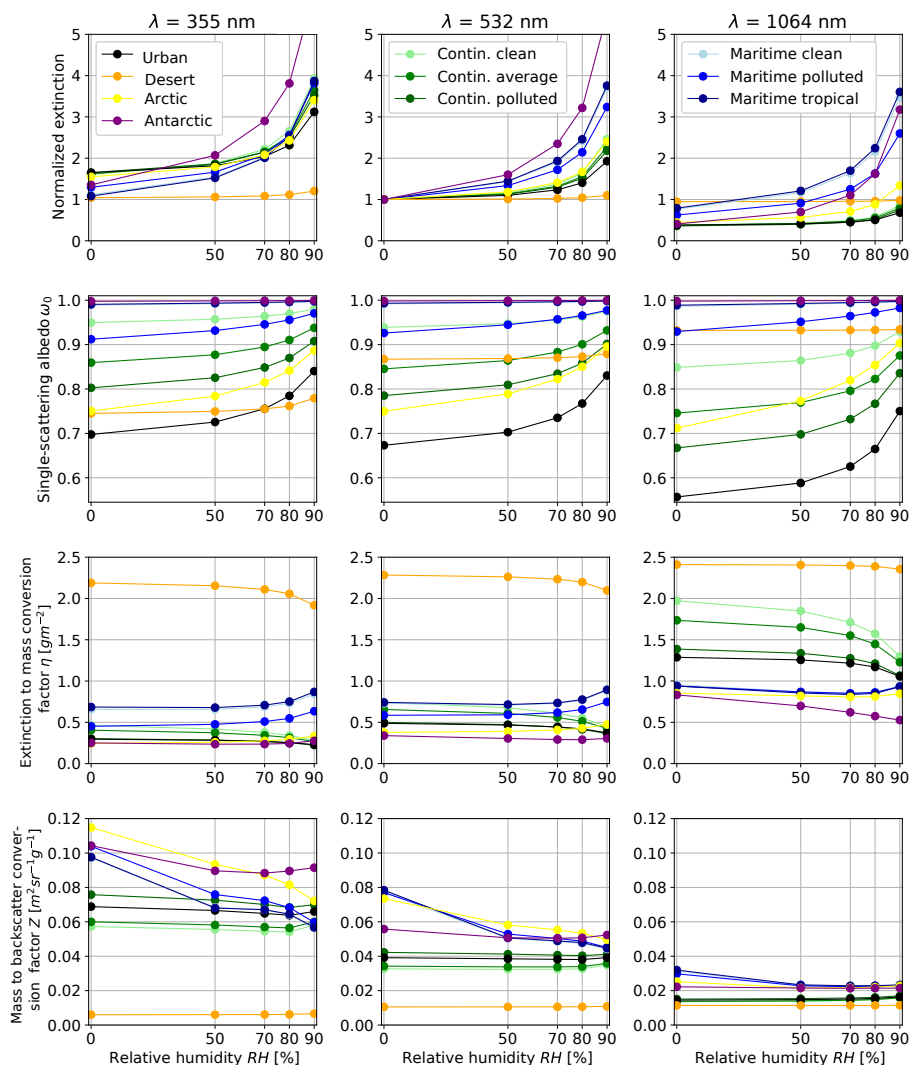
Figure 5. Properties of OPAC aerosol types as a function of relative humidity RH calculated with the κ parameterization (Zieger et al., 2013) implemented in MOPSMAP (Eq. 21). The different colors denote the 10 different OPAC aerosol types as indicated in the legends. The columns denote different wavelengths λ as indicated above the upper row. The upper row shows the extinction coefficient normalized to the extinction coefficient of the same aerosol type at RH = 0 % and $\lambda = 532$ nm. The single-scattering albedo ω_0, the extinction-to-mass conversion factor η, and the mass-to-backscatter conversion factor Z are plotted in the subsequent rows.

Moreover, optical modeling is essential for many different related modeling activities. It is required, for example, for closure experiments (consistency checks between different measurement methods involving an aerosol model, e.g., Wiegner et al., 2009; Gasteiger et al., 2011b; Müller et al., 2012; Bell et al., 2013; Ma et al., 2014; Zieger et al., 2014; Düsing et al., 2018), radiative transfer studies (e.g., Otto et al., 2009; Emde et al., 2010), the inversion of remote-sensing measurements (e.g., Dubovik et al., 2006; Gasteiger et al., 2011a; Müller et al., 2016), the inversion of in situ data (e.g., Weinzierl et al., 2009; Szymanski et al., 2009; Kassianov et al., 2014), aerosol layer visibility simulations (e.g., Weinzierl et al., 2012), dynamic aerosol transport models (e.g., Heinold et al., 2007; Balzarini et al., 2015), aerosol characterization (e.g.,

Gasteiger et al., 2017; Che et al., 2018; Zhuang et al., 2018), and solar energy (e.g., Polo et al., 2016; Kosmopoulos et al., 2017).

5.1 Effect of hygroscopicity

The first example of applications deals with hygroscopic growth. If aerosol particles are hygroscopic, their microphysical and optical properties change with RH. Fig. 5 shows how optical properties of the 10 OPAC aerosol types (Hess et al., 1998), which contain up to four components, some of which are hygroscopic, change with RH. These calculations were performed using the MOPSMAP web interface, where the OPAC aerosol types are available as predefined ensem-

bles and the relative humidity can be chosen by the user. MOPSMAP considers the hygroscopic effect by application of the κ parameterization (Eq. 21), which differs from the RH dependency implemented in OPAC.

The upper row of Fig. 5 shows the normalized extinction coefficient of the different types (indicated by color) at three wavelengths λ (each in a subplot) calculated for RH values of 0, 50, 70, 80, and 90 %. The extinction at all λ is normalized to the extinction at RH = 0 % and λ = 532 nm. As a consequence, the differences between the columns illustrate the wavelength dependency of the extinction, whereas changes with RH illustrate the hygroscopic effects. For example, for the desert aerosol type (orange color), the wavelength dependency is low, which is related to the large size of the dominant mineral particles, and the hygroscopic effect is relatively weak because mineral particles are hygrophobic. By contrast, for maritime (bluish colors) and antarctic types (purple color), the wavelength dependence is stronger and the hygroscopic effect is strong because of the domination by highly hygroscopic sulfate and sea salt particles. For the continental as well as the urban and arctic types, the wavelength dependence is even stronger and the hygroscopic effect weaker, which may be explained by strong contributions from the soot and water-soluble components which contain quite small particles with κ values significantly smaller than the κ values of sea salt particles (e.g., Petters and Kreidenweis, 2007; Markelj et al., 2017; Enroth et al., 2018; Psichoudaki et al., 2018).

The single-scattering albedo ω_0 is shown in the second row of Fig. 5. ω_0 varies strongly with aerosol type, with the highest values of almost 1.0 for the antarctic, maritime clean, and maritime tropical aerosol types. Since water is almost non-absorbing at the considered wavelengths, the water uptake hardly changes ω_0 if ω_0 is already close to 1.0. The single-scattering albedo of the desert type is much lower, but it is also virtually independent on the RH as this aerosol type does not take up much water. For the other types, an increase in RH results in an increase in ω_0.

The extinction-to-mass conversion factor η, which is plotted in the third row of Fig. 5, is necessary to calculate mass concentrations from extinction coefficient measurements or mass loadings from AOD measurements. An important parameter for η is the particle size (e.g., Gasteiger et al., 2011a) with the consequence that the desert aerosol type, which contains the highest fraction of coarse particles of the considered types, shows the highest η values. Again, the wavelength dependency is significant for the other aerosol types so that the η values at λ = 1064 nm (right column) are significantly larger than at λ = 532 nm (middle column). The dependence of η on RH is significantly weaker than the dependence of the extinction on RH (upper row), which may be explained by the increase in mass with increasing RH compensating for the increase in extinction.

The bottom row of Fig. 5 illustrates the mass-to-backscatter conversion factor Z as a function of RH. Z is use-

ful, for example, for comparisons of vertical profiles simulated with aerosol transport models to profiles measured with lidar or ceilometer. The multiplication of simulated aerosol mass concentration M with Z provides simulated β profiles which can be compared with the measurements. The figure shows that there is considerable spread between the different aerosol types, in particular at short wavelengths. RH only has strong effects on the maritime and arctic aerosol types.

Currently the hygroscopic growth of different aerosol components is not ultimately understood, and different κ-values are discussed. With MOPSMAP their influence on the optical properties can easily be determined and used in validation studies.

5.2 Optical properties for sectional aerosol models

Aerosol transport models in combination with the optical properties of the aerosol allow one to model the radiative effect of the aerosol. The aerosol is typically modeled in terms of mass concentrations for a limited number of aerosol types divided over a few size bins (sectional aerosol model) or a few modes (modal aerosol models). Thus, realistic optical properties for each size bin of each aerosol type are required for modeling the radiative effects (e.g., Curci et al., 2015).

In this example, we calculated the optical properties of dust at λ = 500 nm for the five size bins of the COSMO-MUSCAT model (Heinold et al., 2007). The size bins are determined by the radius limits 0.1, 0.3, 0.9, 2.6, 8, and 24 μm. We assumed constant dv/dln$r$ within each bin. Each bin was modeled through the expert mode of the MOPSMAP web interface. The refractive index is $m = 1.53 + 0.0078i$, which is equal to the value given for the mineral components in OPAC. We considered two cases for the particle shape: on the one hand, spherical particles and, on the other hand, prolate spheroids with the aspect ratio distribution given by Kandler et al. (2009). For the latter case we assumed volume-equivalent sizes to keep the particle mass constant.

The calculated phase functions are presented in Fig. 6, where each size bin is represented by an individual color. The difference between both lines of the same color represents the shape effect. For size bin 1 (0.1 μm < r < 0.3 μm, black lines), the difference is small, whereas for all other bins the shape effect is larger. The strongest effects are found for $\theta > 100°$ with differences of up to a factor of 4 between the particle shapes. These angular ranges can be important, for example, for the backscattering of sunlight into space and thus for the aerosol radiative effect. The very strong effect at $\theta = 180°$ is relevant for any lidar application, e.g, the intercomparison of modeled and measured attenuated backscatter profiles (Chan et al., 2018).

Calculated parameters relevant for radiative transfer and remote sensing are given in Table 4. The shape effect on the single-scattering albedo ω_0 and the asymmetry parameter g is small except for size bin 2 where g is significantly larger for the spheroids than for the spheres. The extinction-to-mass

Table 4. Optical properties at $\lambda = 500$ nm of the five COSMO-MUSCAT dust size bins. Two cases for the particle shape are considered: spheres/prolate spheroids. For details, see text.

	Bin 1	Bin 2	Bin 3	Bin 4	Bin 5
ω_0	0.9632/0.9628	0.9216/0.9264	0.7903/0.7934	0.6450/0.6485	0.5561/0.5601
g	0.6567/0.6585	0.6866/0.7111	0.8088/0.8109	0.8998/0.9017	0.9442/0.9419
η (g m^{-2})	0.2905/0.3000	0.5594/0.5236	2.230/2.071	6.989/6.633	22.09/20.90
Z (m^2 sr^{-1} g^{-1})	4.234×10^{-2}/ 3.981×10^{-2}	1.185×10^{-1}/ 5.421×10^{-2}	1.403×10^{-2}/ 8.901×10^{-3}	1.204×10^{-3}/ 7.457×10^{-4}	8.225×10^{-5}/ 8.651×10^{-5}
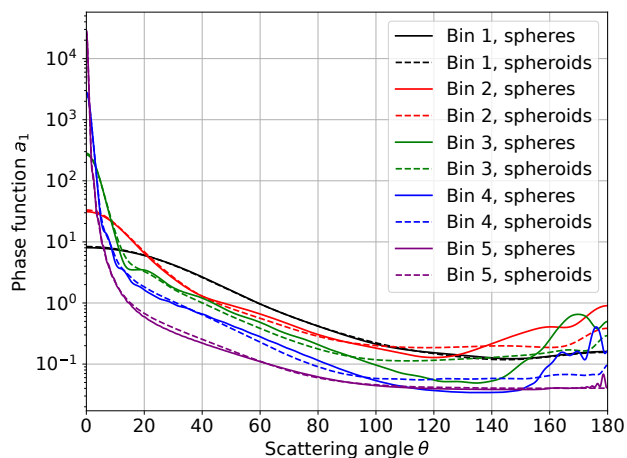
Figure 6. Phase functions at $\lambda = 500$ nm of the five COSMO-MUSCAT dust size bins (different colors) assuming spherical particles (solid lines) and prolate spheroids (dashed lines). For details, see text.

conversion factor η is systematically smaller for spheroids than for spheres in bins 2–5 because the geometric cross section of the spheroids is $\approx 5.5\%$ larger than the cross section of the volume-equivalent spheres. The mass-to-backscatter conversion factor Z of the spheroids is lower than the Z of spheres for most size bins, with maximum differences being larger than a factor of 2.

5.3 Effect of cutoff at maximum size

Many in situ measurement setups are limited with respect to the maximum particle size they are able to sample, e.g., because of losses at the inlet or the tubing. In this example, we illustrate the effect of the cutoff for the desert aerosol type from OPAC at RH = 0 % (Koepke et al., 2015).

Figure 7 illustrates various aerosol properties as a function of the cutoff radius r_{max}. Fig. 7a shows properties that are normalized by the values found at $r_{max} = 60$ μm (where 99.988 % of the total particle cross section is covered, referring to $r_{max} = \infty$). The PM$_{10}$ mass, i.e., the mass in the particles with diameter smaller than 10 μm ($r_{max} = 5$ μm), and the PM$_{2.5}$ mass ($r_{max} = 1.25$ μm) are standard parameters to quantify pollution (e.g., Querol et al., 2004). In our example,
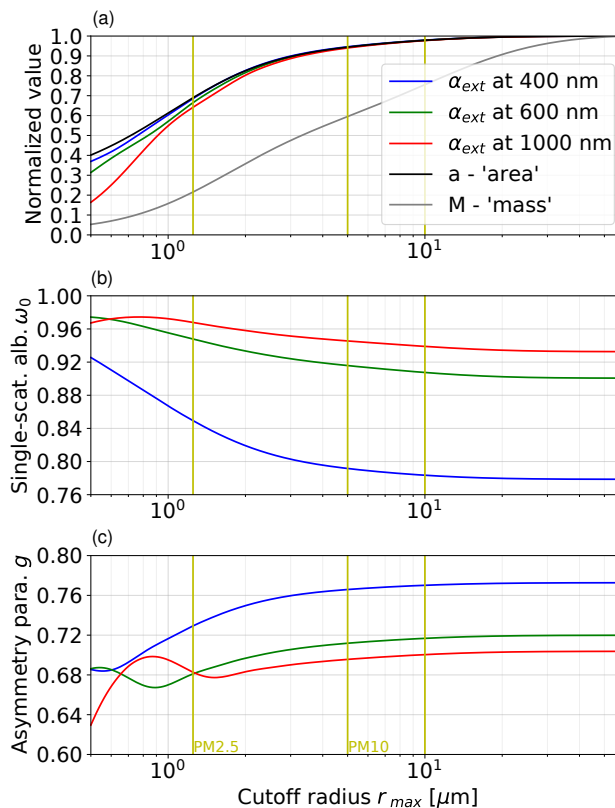
Figure 7. Optical and microphysical properties of the OPAC desert aerosol type as a function of cutoff radius r_{max}. Panel **(a)** shows the normalized extinction coefficient α_{ext} at three wavelengths, the normalized cross section density a, and the normalized mass concentration M. Normalization to values calculated for $r_{max} = 60$ μm. The single-scattering albedo ω_0 at the same wavelengths is plotted in **(b)**, and the asymmetry parameter g in **(c)**.

PM$_{10}$ and PM$_{2.5}$ contain only 59.5 and 21.6 % of the total particle mass, respectively. However, PM$_{10}$ and PM$_{2.5}$ measurement setups cover 94.4 and 69.0 % of the total geometric cross section, respectively. The single-scattering albedo in the case of PM$_{2.5}$ is about 0.035–0.071 higher than for the total aerosol, whereas the asymmetry parameter is reduced by about 0.02–0.04. As a further example, if the cutoff is $r_{max} = 10$ μm, 97.8 % of the total cross section and 75.6 %

Table 5. Properties of one-modal size distribution at $\lambda = 532$ nm consisting of spheres or aggregate particles (shape D, $\xi_{vc} = 0.8708$; Fig. 1 of Gasteiger et al., 2011b) assuming different size equivalences. For details, see text.

| Properties	Spheres	Aggregate particles		
	Using r	Using r_c	Using r_v	Using r_{vcr}
α_{ext} (km^{-1})	0.350	0.347	0.449	0.750
ω_0	0.897	0.922	0.910	0.883
g	0.722	0.679	0.680	0.689
$a_1(0°)$	100	97.4	128	222
$\widetilde{a}_1(0°)$ (km^{-1} sr^{-1})	2.51	2.48	4.17	11.7
$a_1(180°)$	1.21	0.405	0.420	0.432
S (sr)	11.6	33.6	32.8	33.0
δ_l	0.000	0.450	0.454	0.454
Cross section density a (km^{-1})	0.141	0.141	0.186	0.323
Mass concentration M (µg m^{-3})	482	318	481	1103

of the mass are covered; the single-scattering albedo and the asymmetry parameter deviate from the total aerosol by less than 0.008.

This example shows that consideration of maximum size is essential when derived optical properties or mass concentrations are interpreted, and results can be severely misleading if the cutoff radius is not considered. These effects can be easily quantified with MOPSMAP and its web interface.

5.4 Effect of the selection of size equivalence of nonspherical particles

This example demonstrates how the selection of the size equivalence in the case of nonspherical particles affects various ensemble properties. In MOPSMAP the size-related parameters are either interpreted as r_c (default) or as r_v or r_{vcr} (see Sect. 2.1) according to the choice of the user. Each size equivalence can be transformed into another by Eqs. (3) and (4). For example, if "volume cross section ratio equivalent" has been chosen in the web interface, and "0.5" for r_{mod}, this would be equivalent to setting $0.5 \cdot \xi_{vc}^{-3}$ for r_{mod} when the default "cross section equivalent" is kept (ξ_{vc} depending on shape).

To further elucidate the role of the different representations of radii, the same parameters of a lognormal size distribution are applied to the different size interpretations. For this purpose, the parameters are set to $r_{mod} = 0.5$ µm and $\sigma = 2$ with $r_{min} = 0.001$ µm, $r_{max} = 1.75$ µm ($r_{eff} = 0.98$ µm), and $N_0 = 103.66$ cm^{-3}, which results in a concentration of $N = 100$ cm^{-3} in the range from r_{min} to r_{max}. The effect of the three alternative interpretations on particle size is demonstrated in Fig. 8 for irregular shape D having $\xi_{vc} = 0.8708$. All three size distributions (curves of different color) are plotted in terms of $dN/dr_c(r_c)$ (black axes). For comparison, axes for $dN/dr_v(r_v)$ (red axes) and $dN/dr_{vcr}(r_{vcr})$ (green axes) are also shown. Using these axes, the size distribution curves can be interpreted in terms of the various size equiva-
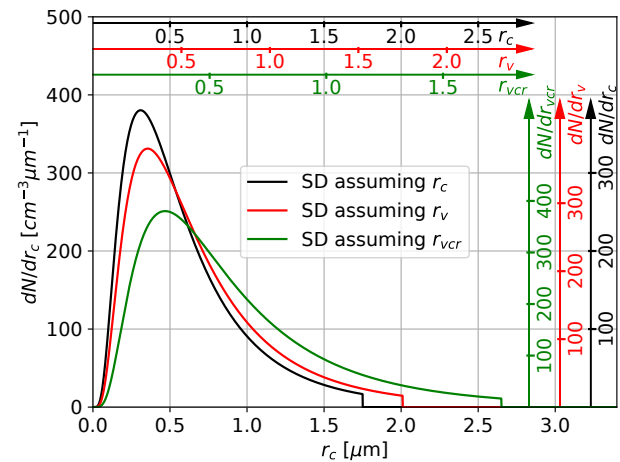
Figure 8. Lognormal size distributions (SD) with same r_{mod}, σ, N_0, and r_{max} assuming different size equivalences for aggregate particles (shape D, $\xi_{vc} = 0.8708$) as applied in Table 5. The size distributions are plotted in terms of cross-section-equivalent sizes (i.e., $dN/dr_c(r_c)$ referring to black axes and grid). For comparison axes valid for the other size interpretations are also plotted in red and green, which allows each size distribution to be interpreted in terms of each size equivalence.

lences. The comparison between the size distributions clearly shows a shift towards larger sizes when r_{vcr} or r_v instead of r_c is assumed. For example, assuming r_{vcr} for the lognormal size distribution (green curve) describes the same ensemble as using $r_{mod} = \xi_{vc}^{-3} \cdot 0.5$ µm $= 0.8708^{-3} \cdot 0.5$ µm $= 0.757$ µm (see Eq. 4) and $r_{max} = 0.8708^{-3} \cdot 1.75$ µm $= 2.65$ µm when assuming r_c as particle size.

Since the size distributions depend on the selected size equivalence various (optical) properties of the ensemble are also different; a quantification has been provided by MOPSMAP (Table 5). The particle mass density is set to 2600 kg m^{-3}, the refractive index is $m = 1.54 + 0.005i$ and the wavelength is $\lambda = 532$ nm. The first column of Table 5

shows the optical properties of spherical particles. In the subsequent columns, all particles are assumed to be aggregate particles (shape D) with the same r_c (second column, corresponding to the black curve in Fig. 8), the same r_v (third column, red curve), and the same r_{vcr} (last column, green curve) as the spheres in the first column.

The results are consistent with the increase in particle size from assuming r_c over r_v to r_{vcr} (see cross section density a, mass concentration M, and also Fig. 8). The extinction coefficient α_{ext} and the forward volume scattering $\widetilde{a}_1(0°)$ of the nonspherical particles best agree with the spherical counterparts if cross section equivalence is assumed. These properties are known to be sensitive to the particle cross section for particles larger than the wavelength. The absorption is in first approximation proportional to the particle volume if absorption is weak. As a consequence, for the single-scattering albedo ω_0, both cross section and volume are relevant and dependencies are more complicated than for α_{ext}. The single-scattering albedo ω_0 of shape D decreases in Table 5 from left to right due to the strong increase in particle volume. The selection of the size equivalence has a small effect on the asymmetry parameter g, the backward phase function $a_1(180°)$, the lidar ratio S, and the linear depolarization ratio δ_l.

These results highlight the importance of a thoughtful selection of the size equivalence. The most appropriate size equivalence certainly depends on the concept of how the size distribution is measured. For example, if scattering by coarse dust particles is measured and the size is inverted assuming spherical particles, assuming cross-section equivalence in subsequent applications with nonspherical particles seems natural as scattering mainly depends on the particle cross section. MOPSMAP and its web interface provides the flexibility to investigate this topic theoretically.

5.5 Uncertainty estimation of calculated optical properties

In general, the knowledge on microphysical properties is limited; thus, they are subject to uncertainties. If these uncertainties can be quantified, it is consistent to also quantify the corresponding uncertainties of the optical properties.

In this regard, the sensitivity of a calculated optical property ζ to changes in a microphysical property ψ is an important aspect that can be expressed by the first partial derivative $\partial\zeta/\partial\psi$. The Jacobian matrix $\mathbf{J}$ is the $M \times N$ matrix containing all first partial derivatives for M optical properties and N microphysical properties. The elements of $\mathbf{J}$ of an aerosol ensemble can be numerically calculated by perturbing the microphysical properties of the ensemble. For demonstration in the following example we perturb ψ with a factor of 0.99 and 1.01 to numerically calculate the first partial derivatives. A sample script for the calculation of $\mathbf{J}$ is provided together with MOPSMAP.

Table 6 shows an example of $\mathbf{J}$ for the optical properties $\zeta \in \{\omega_0, g, S\}$ and the microphysical properties $\psi \in$

Table 6. Elements of the Jacobian matrix, i.e., first partial derivatives, of a dust-like ensemble (see text for details).

	$\partial\omega_0$	∂g	∂S
∂m_r	-0.037	-0.428	-360 sr
∂m_i	-11.0	$+3.69$	$+2839$ sr
$\partial\epsilon'$	$+0.010$	$+0.058$	$+48.3$ sr

$\{m_r, m_i, \epsilon'\}$. $\mathbf{J}$ was calculated for a simplified dust ensemble described by one lognormal size mode with $r_{mod} = 0.1$ μm, $\sigma = 2.6$, $r_{min} = 0.001$ μm, $r_{max} = 20$ μm, a refractive index $m = 1.53 + 0.0063i$, and prolate spheroids with $\epsilon' = 2.0$. The wavelength is set to $\lambda = 532$ nm. This results in $\omega_0 = 0.9020$, $g = 0.7319$, and $S = 69.95$ sr. These properties are most sensitive to m_i, which can be clearly seen from Table 6. For example, a change in m_i by 0.001 would result in a change in ω_0 of 0.011. An increase in ϵ' or m_i increases g and S, whereas an increase in m_r reduces their values. The sensitivity to perturbations of the microphysical properties is particularly strong for the lidar ratio S, which can be seen by comparing $S = 69.95$ sr of the ensemble with the partial derivatives. We emphasize that the accuracy of $\mathbf{J}$ is limited by the sampling in the MOPSMAP data set (see also Sect. 3.3); for example, partial derivatives $\partial\zeta/\partial m_r$ are constant between the m_r grid points of the data set.

The Jacobian matrix $\mathbf{J}$ is valid for a certain set of microphysical properties values and, as mentioned, $\mathbf{J}$ can be used to quantify the uncertainty of the calculated properties for a given microphysical uncertainty. However, when uncertainties in the microphysical properties become larger, $\mathbf{J}$ may change significantly within the uncertainty range of ψ and other approaches may be required to estimate the uncertainty in the calculated optical properties. A simple approach applicable to this problem is the Monte Carlo method (e.g., JCGM, 2008). Repeated calculations with microphysical properties randomly chosen within the uncertainty range are performed. The uncertainty of the calculated quantities is determined by the statistics over the different sampled ensembles. In general, the computation time is longer than using $\mathbf{J}$ and is proportional to the number of calculated ensembles. Due to the statistical nature of the Monte Carlo method, the final results get more precise with increasing number of sampled ensembles. A script for the Monte Carlo uncertainty propagation is provided together with MOPSMAP. For example, based on the ensemble described above, sampling within the uncertainty ranges $r_{mod} = 0.1 \pm 0.01$ μm, $\sigma = 2.6 \pm 0.1$, $m_r = 1.53 \pm 0.03$, $m_r = 0.0063 \pm 0.002$, and $\epsilon' = 2.0 \pm 0.5$ results in the ranges $0.85 < \omega_0 < 0.94$, $0.68 < g < 0.78$, and 29 sr $< S < 103$ sr.

5.6 Effect of refractive index variability

Mineral dust aerosols are ensembles of different minerals with different refractive indices. Usually the variability in the
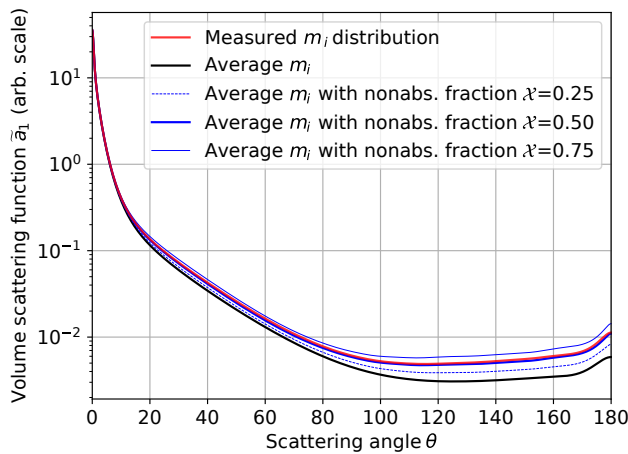
Figure 9. Volume scattering function of dust at $\lambda = 355$ nm (arbitrary scale) using either the m_i distribution (red) measured by Kandler et al. (2011), the average m_i of these measurements (black), or applying the non-absorbing fraction parameterization with different $\mathcal{X}$ (blue).

refractive index of the particles within a dust aerosol ensemble is neglected when modeling its optical properties. In this example, we compare optical properties calculated using the full measured variability in the imaginary part of the refractive index m_i to properties calculated with the common assumption of all particles in an ensemble having an average m_i. Furthermore, a parameterization of the variability is considered.

We use the desert aerosol type of OPAC (Koepke et al., 2015). Prolate spheroids with the aspect ratio distribution of Kandler et al. (2009) are assumed for the mineral components and spherical particles for the WASO component (RH = 0 %). The real part of the refractive index is $m_r = 1.53$ for all particles. The wavelength in this example is set to $\lambda = 355$ nm, which is a wavelength where absorption by iron oxide is strong. Because of the variable iron oxide content of individual particles, the variability in m_i is large at this wavelength. Consequently, a significant influence on optical properties can be expected. In this example we consider three cases of imaginary part variability: first, we apply the size-resolved distribution of the imaginary part of the refractive index for Saharan dust as derived from mineralogical analysis (Kandler et al., 2011). Second, we assume the average imaginary part for all particles (it is 0.0175, which is close to 0.0166 given for the mineral components in OPAC at $\lambda = 355$ nm). Finally, we parameterize the m_i distribution with the non-absorbing fraction approach as introduced in Sect. 3.1. In this case, we set $\mathcal{X} = 0.5$, resulting in 50 % of the mineral particles having $m_i = 0$, whereas the other 50 % of the particles have $m_i = 0.0349$.

Figure 9 shows the volume scattering function for the three cases. This figure shows that the sensitivity of the forward scattering to the m_i distribution is negligible whereas the

sensitivity increases with increasing scattering angle θ. For backward scattering, the difference between the measured m_i distribution (red line) and using the average m_i (black line) is more than a factor of 2. The parameterization assuming $\mathcal{X} = 0.5$ (thick blue line) is in much better agreement with the measured case. The root-mean-square relative deviation between the volume scattering function for the measured distribution and for the average m_i is 30 %, whereas it is only 4 % for the parameterization. For comparison two additional $\mathcal{X}$ values, i.e., $\mathcal{X} = 0.25$ (thin dashed blue line) as well as $\mathcal{X} = 0.75$ (thin solid blue line), are also shown in Fig. 9, but their deviation is larger than for the parameterization with $\mathcal{X} = 0.5$. The extinction coefficient α_{ext} only changes by less than 0.03 % between the three representations of m_i. For ω_0 we obtain 0.852 using the measured m_i distribution, whereas $\omega_0 = 0.741$ when using the average m_i and $\omega_0 = 0.834$ using the parameterization with $\mathcal{X} = 0.5$. For the asymmetry parameter g, we obtain 0.744, 0.789, and 0.749 for the measured, averaged, and parameterized cases, respectively. For the lidar ratio S, values of 41, 78, and 42 sr are calculated for the three cases, whereas for the linear depolarization ratio δ_l values of 0.241, 0.212, and 0.220 are obtained.

These results emphasize that it is important to consider the nonuniform distribution of the absorptive components in the desert dust ensembles for optical modeling of such aerosols at short wavelengths. We have shown in this example that optical properties of Saharan dust can be well simulated with $\mathcal{X} = 0.5$. Whether this conclusion holds for other cases of desert dust can easily be investigated by means of MOPSMAP when measurements of m_i distributions of further dust types are available.

5.7 Effect of particle shape on the nephelometer truncation error

Integrating nephelometers aim to measure in situ the total scattering coefficient $\alpha_{\text{sca}}^{\text{true}}$ of aerosol particles by detecting all scattered light. The angular sensitivities of real nephelometers, however, deviate from the ideal sensitivity, which is the sine of scattering angle θ. For example, nearly forward or nearly backward scattered light does not reach the detectors because of the instrument geometry (Müller et al., 2011). This has to be considered during the evaluation of measurements and can be done by applying a truncation correction factor $C_{\text{ts}} = \alpha_{\text{sca}}^{\text{true}} / \alpha_{\text{sca}}^{\text{meas}}$ to the measured scattering coefficients $\alpha_{\text{sca}}^{\text{meas}}$. C_{ts} can be calculated theoretically using optical modeling if aerosol microphysical properties and the angular sensitivity of the instrument are known. Some nephelometers not only measure the total scattering coefficient but also the hemispheric backscattering coefficient, which is the scattering integrated from $\theta = 90$ to $180°$. For the hemispheric backscattering coefficient, a correction factor also needs to be applied to correct the measured hemispheric backscattering coefficient affected by the nonideal instrument sensitivity. This correction factor C_{bs} is defined analogously to C_{ts}
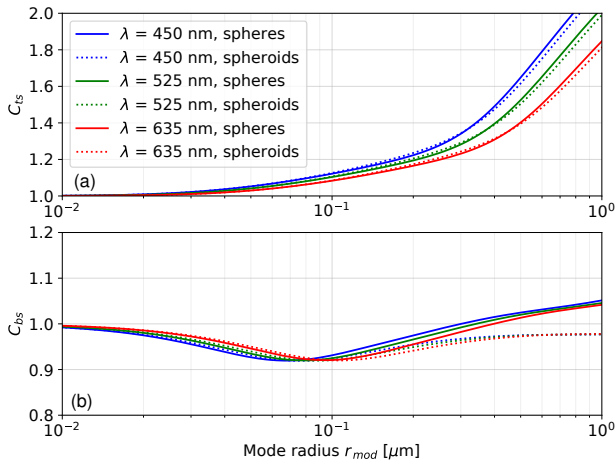
Figure 10. Modeled correction factors C_{ts} for total scattering **(a)** and C_{bs} for hemispheric backscattering **(b)** of an Aurora 3000 nephelometer as a function of particle size. For details, see text.

as the ratio between the true coefficient and the measured one. Note that this hemispheric backscattering coefficient is defined differently from β, which is measured by lidars and used elsewhere in this paper.

Figure 10 shows modeled correction factors for the total (Fig. 10a) and the backscatter (Fig. 10b) channel of an Aurora 3000 nephelometer. The angular sensitivity of the instrument is taken from Müller et al. (2011). For the following sensitivity study the mineral dust refractive index from OPAC (Hess et al., 1998), the parameterized m_i distribution with $\mathcal{X} = 0.5$ (as shown in Sect. 5.6), a lognormal size mode with $\sigma = 1.6$ and a maximum radius of $r_{max} = 5\,\mu m$ (corresponding to a PM$_{10}$ inlet) is assumed. The mode radius r_{mod} is varied from 0.01 to 1 µm (horizontal axis) and two cases for the particle shape, i.e., spherical particles (solid lines) and cross-section-equivalent prolate spheroids with the ϵ' distribution from Kandler et al. (2009) (dashed lines), are considered. The colors denote the three operating wavelengths of the instrument (450, 525, and 635 nm). The figure shows that the total scattering correction factor C_{ts} mainly depends on particle size. In the case of large particles ($r_{mod} = 1\,\mu m$), the nephelometer underestimates total scattering by a factor of ≈ 2 if the truncation error is not corrected. Shape only has a small effect on forward scattering; thus, its influence on the correction of the truncation error is less than 3 % (compare dashed and solid lines of the same color). The maximum shape effect on C_{bs} is 7 %, i.e., indicating that assuming spherical particles for the truncation correction may result in an overestimation of the hemispheric backscattering coefficient.

The correction factors might be recalculated for example when new data on the refractive index or particle shape become available. This example highlights the potential of MOPSMAP as a useful tool for the characterization of opti-

cal in situ instruments. In addition, it could be used for the interpretation of angular measurements, for example, as performed with a polar photometer by Horvath et al. (2006).
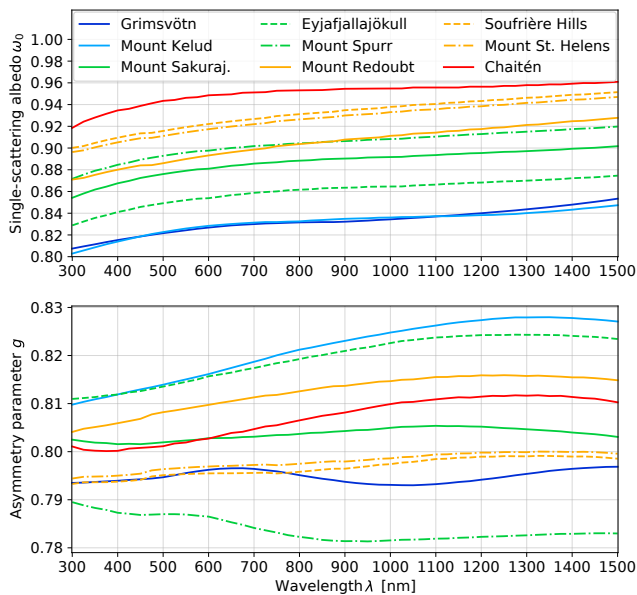
5.8 Optical properties of ash from different volcanoes close to the source

Vogel et al. (2017) present a data set comprising shape–size distributions of ashes from nine different volcanoes as well as wavelength-dependent refractive indices for five different ash types. The particles were collected between 5 and 265 km from the volcanoes. While refractive indices can also be expected to be valid at larger distances from the volcanoes, the effective radii in the range from 9.5 to 21 µm are probably not realistic for long-range-transported ash. Based on this data set, which is available in the supporting information of Vogel et al. (2017), we calculate optical properties of these volcanic ashes with MOPSMAP. Each single particle is modeled as a prolate spheroid with the given size and aspect ratio, as well as with the refractive index given for the type of ash the volcano emits. In addition, we assume a non-absorbing fraction of $\mathcal{X} = 0.5$ (as used in Sect. 5.6). The application of this non-absorbing fraction approach seems reasonable when taking into account the variability in the transparency of the particles shown in Fig. 5 of Vogel et al. (2017). Due to the data set limits of MOPSMAP, particles with $r > 47.5\,\mu m$ are modeled as $r = 47.5\,\mu m$ and aspect ratios > 5 are set to 5. For each volcano, less than 0.5 % of the particles was affected by these modifications.

Figure 11 shows the single-scattering albedo ω_0 and the asymmetry parameter g for the nine ashes as a function of wavelength between 300 and 1500 nm. Differences of ω_0 are up to about 0.12 with ash from Chaitén (Chile) and Mt. Kelud (Indonesia) being the least and most absorbing species, respectively. ω_0 is correlated with the ash type, which is mainly a result of the significant variability in m_i (see Fig. 16b of Vogel et al., 2017). For all ashes, ω_0 increases slightly with wavelength, typically by about 0.05 over the wavelength range shown. The variability in g is less than 0.05, and for all ashes the changes with wavelength are weak with values of less than 0.02. The mass-to-backscatter conversion factor Z varies between 1.16 and $3.38 \times 10^{-3}\,m^2\,sr^{-1}\,g^{-1}$ for the nine ashes. The extinction-to-mass conversion factor η at $\lambda = 550\,nm$ ranges from 14.8 to 33.0 g m^{-2} which is considerably higher than known for typical aerosols (e.g., Fig. 5) or volcanic ash transported over continental scales (e.g., η between 1.10 and 1.88 g m^{-2} found by Wiegner et al., 2012). In particular the different values of η clearly demonstrate that optical properties of volcanic ash layers drastically change with the distance from the eruption due to changing microphysics.

This example suggests that it is worthwhile considering the specific microphysical properties of each volcano. However, for realistic MOPSMAP calculations valid in the long-range regime, size distributions different from the ones used

Figure 11. Modeled wavelength-dependent optical properties for ashes from different volcanoes. More details on the ash samples are given in Table 1 of Vogel et al. (2017). The colors indicate ash type: basalt is dark blue, basaltic andesite is light blue, andesite is green, dacite is orange, and rhyolite is red (see Fig. 7 of Vogel et al., 2017 for reference).

in this example must certainly be applied whereas the refractive indices are more likely representative.

6   Conclusions

Radiative properties of atmospheric aerosols are relevant for a wide range of meteorological applications, in particular for radiative transfer calculations and remote-sensing and in situ techniques. Optical properties strongly depend on the microphysical properties of the particles – size, refractive index and shape – properties that are highly variable under ambient conditions. As a consequence, the application of mean properties could be questionable. However, the determination of optical properties of specific aerosol ensembles can be quite time-consuming, in particular when nonspherical particles shall be considered.

For this purpose we have developed the MOPSMAP package that provides the full set of optical properties of arbitrary, randomly oriented aerosol ensembles: single particles of the ensemble can be spherical or spheroidal with size parameters up to $x \approx 1000$. Moreover, a small set of irregular particles is considered. The refractive index can be $0.1 \leq m_r \leq 3.0$ and $0 \leq m_i \leq 2.2$. The size distribution of the ensemble can either be parameterized as a lognormal distribution, as a (modified) gamma distribution, or freely chosen according to individual data. MOPSMAP includes a web interface for online calculations at https://mopsmap.net, offering the

most frequently used options; for advanced applications or large sets of computations, the full package is freely available for download. Key applications of MOPSMAP are expected to be the evaluation of radiometer measurements in the UV, VIS and near-infrared spectral range or aerosol lidar measurements. They can help to improve the inversion of such measurements for aerosol characterization. Furthermore, MOPSMAP can be used to refine optical properties of aerosols in radiative transfer models or in numerical weather prediction and chemistry transport models.

The details of the concept underlying MOPSMAP are discussed in this paper. Several examples are presented to illustrate the potential of the package, including an example to calculate optical properties for sectional aerosol models and an example illustrating the effect of maximum size cutoff that occurs in the inlet system of in situ instruments. In another example, conversion factors between the backscatter coefficient (available from lidar/ceilometer measurements or from numerical forecast models) and the mass concentration of volcanic ashes have been calculated. These conversion factors are relevant to estimate flight safety after volcanic eruptions and vary by about a factor of 3 between the nine ashes under investigation.

The concept of MOPSMAP allows continuous upgrades to further extend the range of applications. For example, the resolution of the refractive index grid could be increased, new versions of underlying scattering codes could be applied when available, larger size parameters could be considered, e.g., using DDA for m close to 1 (Yurkin and Hoekstra, 2011), and new sets of irregular particles could be implemented, e.g., those presented by Mehri et al. (2018). However such extensions can be quite time-consuming, so that extensions are expected to be limited. Moreover, conceptional upgrades will be investigated without knowing yet whether they can be included in the web interface. Here, a trade-off between scientific complexity and user-friendliness must be found. Whereas internal mixing in the case of homogeneous particles is already covered in the present version, the implementation of a core-shell particle model can be discussed. Finally, we want to emphasize that the feedback from the users will help us to set up a priority list of further actions.

References

Baklanov, A., Schlünzen, K., Suppan, P., Baldasano, J., Brunner, D., Aksoyoglu, S., Carmichael, G., Douros, J., Flemming, J., Forkel, R., Galmarini, S., Gauss, M., Grell, G., Hirtl, M., Joffre, S., Jorba, O., Kaas, E., Kaasik, M., Kallos, G., Kong, X., Korsholm, U., Kurganskiy, A., Kushta, J., Lohmann, U., Mahura, A., Manders-Groot, A., Maurizi, A., Moussiopoulos, N., Rao, S. T., Savage, N., Seigneur, C., Sokhi, R. S., Solazzo, E., Solomos, S., Sørensen, B., Tsegas, G., Vignati, E., Vogel, B., and Zhang, Y.: Online coupled regional meteorology chemistry models in Europe: current status and prospects, Atmos. Chem. Phys., 14, 317–398, https://doi.org/10.5194/acp-14-317-2014, 2014.

Balzarini, A., Pirovano, G., Honzak, L., Žabkar, R., Curci, G., Forkel, R., Hirtl, M., José, R. S., Tuccella, P., and Grell, G.: WRF-Chem model sensitivity to chemical mechanisms choice in reconstructing aerosol optical properties, Atmospheric Environ., 115, 604 – 619, https://doi.org/10.1016/j.atmosenv.2014.12.033, 2015.

Bell, S. W., Hansell, R. A., Chow, J. C., Tsay, S.-C., Hsu, N. C., Lin, N.-H., Wang, S.-H., Ji, Q., Li, C., Watson, J. G., and Khlystov, A.: Constraining aerosol optical models using ground-based, collocated particle size and mass measurements in variable air mass regimes during the 7-SEAS/Dongsha experiment, Atmos. Environ., 78, 163–173, https://doi.org/10.1016/j.atmosenv.2012.06.057, 2013.

Bi, L., Yang, P., Kattawar, G. W., and Kahn, R.: Single-scattering properties of triaxial ellipsoidal particles for a size parameter range from the Rayleigh to geometric-optics regimes, Appl. Opt., 48, 114–126, https://doi.org/10.1364/AO.48.000114, 2009.

Binkowski, F. S. and Shankar, U.: The Regional Particulate Matter Model: 1. Model description and preliminary results, J. Geophys. Res.-Atmos., 100, 26191–26209, https://doi.org/10.1029/95JD02093, 1995.

Chan, K. L., Wiegner, M., Flentje, H., Mattis, I., Wagner, F., Gasteiger, J., and Geiß, A.: Evaluation of operational model forecasts of aerosol transport using ceilometer network measurements, Geosci. Model Dev. Discuss., https://doi.org/10.5194/gmd-2018-74, in review, 2018.

Che, H., Qi, B., Zhao, H., Xia, X., Eck, T. F., Goloub, P., Dubovik, O., Estelles, V., Cuevas-Agulló, E., Blarel, L., Wu, Y., Zhu, J., Du, R., Wang, Y., Wang, H., Gui, K., Yu, J., Zheng, Y., Sun, T., Chen, Q., Shi, G., and Zhang, X.: Aerosol optical properties and direct radiative forcing based on measurements from the China Aerosol Remote Sensing Network (CARSNET) in eastern China, Atmos. Chem. Phys., 18, 405–425, https://doi.org/10.5194/acp-18-405-2018, 2018.

Chýlek, P.: Resonance structure of Mie scattering: distance between resonances, J. Opt. Soc. Am. A, 7, 1609–1613, https://doi.org/10.1364/JOSAA.7.001609, 1990.

Curci, G., Hogrefe, C., Bianconi, R., Im, U., Balzarini, A., Baró, R., Brunner, D., Forkel, R., Giordano, L., Hirtl, M., Honzak, L., Jiménez-Guerrero, P., Knote, C., Langer, M., Makar, P., Pirovano, G., Pérez, J., José, R. S., Syrakov, D., Tuccella, P., Werhahn, J., Wolke, R., Žabkar, R., Zhang, J., and Galmarini, S.: Uncertainties of simulated aerosol optical properties induced by assumptions on aerosol physical and chemical properties: An AQMEII-2 perspective, Atmos. Environ., 115, 541–552, https://doi.org/10.1016/j.atmosenv.2014.09.009, 2015.

Deirmendjian, D.: Scattering and Polarization Properties of Water Clouds and Hazes in the Visible and Infrared, Appl. Opt., 3, 187–196, https://doi.org/10.1364/AO.3.000187, 1964.

Dubovik, O., Sinyuk, A., Lapyonok, T., Holben, B. N., Mishchenko, M., Yang, P., Eck, T. F., Volten, H., Muñoz, O., Veihelmann, B., van der Zande, W. J., Leon, J., Sorokin, M., and Slutsker, I.: Application of spheroid models to account for aerosol particle nonsphericity in remote sensing of desert dust, J. Geophys. Res., 111, D11208, https://doi.org/10.1029/2005JD006619, 2006.

Düsing, S., Wehner, B., Seifert, P., Ansmann, A., Baars, H., Ditas, F., Henning, S., Ma, N., Poulain, L., Siebert, H., Wiedensohler, A., and Macke, A.: Helicopter-borne observations of the continental background aerosol in combination with remote sensing and ground-based measurements, Atmos. Chem. Phys., 18, 1263–1290, https://doi.org/10.5194/acp-18-1263-2018, 2018.

Emde, C., Buras, R., Mayer, B., and Blumthaler, M.: The impact of aerosols on polarized sky radiance: model development, validation, and applications, Atmos. Chem. Phys., 10, 383–396, https://doi.org/10.5194/acp-10-383-2010, 2010.

Emde, C., Buras-Schnell, R., Kylling, A., Mayer, B., Gasteiger, J., Hamann, U., Kylling, J., Richter, B., Pause, C., Dowling, T., and Bugliaro, L.: The libRadtran software package for radiative transfer calculations (version 2.0.1), Geosci. Model Dev., 9, 1647–1672, https://doi.org/10.5194/gmd-9-1647-2016, 2016.

Enroth, J., Mikkilä, J., Németh, Z., Kulmala, M., and Salma, I.: Wintertime hygroscopicity and volatility of ambient urban aerosol particles, Atmos. Chem. Phys., 18, 4533–4548, https://doi.org/10.5194/acp-18-4533-2018, 2018.

Gardner, G. Y.: Simulation of natural scenes using textured quadric surfaces, Proceedings of the 11th annual conference on Computer graphics and interactive techniques, 11–20, 1984.

Gasteiger, J. and Wiegner, M.: Modeling of aerosol optical properties with MOPSMAP: Fortran program with data set, https://doi.org/10.5281/zenodo.1284217, 2018.

Gasteiger, J., Groß, S., Freudenthaler, V., and Wiegner, M.: Volcanic ash from Iceland over Munich: mass concentration retrieved from ground-based remote sensing measurements, At-

mos. Chem. Phys., 11, 2209–2223, https://doi.org/10.5194/acp-11-2209-2011, 2011a.

Gasteiger, J., Wiegner, M., Groß, S., Freudenthaler, V., Toledano, C., Tesche, M., and Kandler, K.: Modeling lidar-relevant optical properties of complex mineral dust aerosols, Tellus B, 63, 725–741, https://doi.org/10.1111/j.1600-0889.2011.00559.x, 2011b.

Gasteiger, J., Groß, S., Sauer, D., Haarig, M., Ansmann, A., and Weinzierl, B.: Particle settling and vertical mixing in the Saharan Air Layer as seen from an integrated model, lidar, and in situ perspective, Atmos. Chem. Phys., 17, 297–311, https://doi.org/10.5194/acp-17-297-2017, 2017.

Hänel, G. and Zankl, B.: Aerosol size and relative humidity: Water uptake by mixtures of salts, Tellus, 31, 478–486, https://doi.org/10.3402/tellusa.v31i6.10465, 1979.

Heinold, B., Helmert, J., Hellmuth, O., Wolke, R., Ansmann, A., Marticorena, B., Laurent, B., and Tegen, I.: Regional modeling of Saharan dust events using LM-MUSCAT: Model description and case studies, J. Geophys. Res.-Atmos., 112, D11204, https://doi.org/10.1029/2006JD007443, 2007.

Hess, M., Koepke, P., and Schult, I.: Optical Properties of Aerosols and Clouds: The Software Package OPAC, B. Am. Meteorol. Soc., 79, 831–844, https://doi.org/10.1175/1520-0477(1998)079<0831:OPOAAC>2.0.CO;2, 1998.

Hill, S. C., Hill, A. C., and Barber, P. W.: Light scattering by size/shape distributions of soil particles and spheroids, Appl. Opt., 23, 1025–1031, https://doi.org/10.1364/AO.23.001025, 1984.

Holben, B. N., Eck, T. F., Slutsker, I., Tanré, D., Buis, J. P., Setzer, A., Vermote, E., Reagan, J. A., Kaufman, Y. J., Nakajima, T., Lavenu, F., Jankowiak, I., and Smirnov, A.: AERONET – A Federated Instrument Network and Data Archive for Aerosol Characterization, Remote Sens. Environ., 66, 1–16, https://doi.org/10.1016/S0034-4257(98)00031-5, 1998.

Horvath, H.: Gustav Mie and the scattering and absorption of light by particles: Historic developments and basics, J. Quant. Spectrosc. Ra., 110, 787–799, https://doi.org/10.1016/j.jqsrt.2009.02.022, 2009.

Horvath, H., Kasahara, M., Tohno, S., and Kocifaj, M.: Angular scattering of the Gobi Desert aerosol and its influence on radiative forcing, J. Aerosol Sci., 37, 1287–1302, https://doi.org/10.1016/j.jaerosci.2006.01.004, 2006.

Hovenier, J. W. and van der Mee, C. V. M.: Fundamental relationships relevant to the transfer of polarized light in a scattering atmosphere, Astron. Astrophys., 128, 1–16, 1983.

JCGM: Evaluation of measurement data – Supplement 1 to the "Guide to the expression of uncertainty in measurement" – Propagation of distributions using a Monte Carlo method, Tech. rep., Joint Committee for Guides in Metrology, https://www.bipm.org/en/publications/guides/gum.html (last access: 8 July 2018), 2008.

Kahn, R., West, R., McDonald, D., Rheingans, B., and Mishchenko, M. I.: Sensitivity of multiangle remote sensing observations to aerosol sphericity, J. Geophys. Res., 102, 16861–16870, https://doi.org/10.1029/96JD01934, 1997.

Kandler, K., Benker, N., Bundke, U., Cuevas, E., Ebert, M., Knippertz, P., Rodríguez, S., Schütz, L., and Weinbruch, S.: Chemical composition and complex refractive index of Saharan Mineral Dust at Izaña, Tenerife (Spain) derived by electron microscopy, Atmos. Environ., 41, 8058–8074, https://doi.org/10.1016/j.atmosenv.2007.06.047, 2007.

Kandler, K., Schütz, L., Deutscher, C., Ebert, M., Hofmann, H., Jäckel, S., Jaenicke, R., Knippertz, P., Lieke, K., Massling, A., Petzold, A., Schladitz, A., Weinzierl, B., Wiedensohler, A., Zorn, S., and Weinbruch, S.: Size distribution, mass concentration, chemical and mineralogical composition and derived optical parameters of the boundary layer aerosol at Tinfou, Morocco, during SAMUM 2006, Tellus B, 61, 32–50, https://doi.org/10.1111/j.1600-0889.2008.00385.x, 2009.

Kandler, K., Lieke, K., Benker, N., Emmel, C., Küpper, M., Müller-Ebert, D., Scheuvens, D., Schladitz, A., Schütz, L., and Weinbruch, S.: Electron microscopy of particles collected at Praia, Cape Verde, during the Saharan Mineral dust experiment: particle chemistry, shape, mixing state and complex refractive index, Tellus B, 63, 475–496, https://doi.org/10.1111/j.1600-0889.2011.00550.x, 2011.

Kassianov, E., Barnard, J., Pekour, M., Berg, L. K., Shilling, J., Flynn, C., Mei, F., and Jefferson, A.: Simultaneous retrieval of effective refractive index and density from size distribution and light-scattering data: weakly absorbing aerosol, Atmos. Meas. Tech., 7, 3247–3261, https://doi.org/10.5194/amt-7-3247-2014, 2014.

Koepke, P., Gasteiger, J., and Hess, M.: Technical Note: Optical properties of desert aerosol with non-spherical mineral particles: data incorporated to OPAC, Atmos. Chem. Phys., 15, 5947–5956, https://doi.org/10.5194/acp-15-5947-2015, 2015.

Kosmopoulos, P. G., Kazadzis, S., Taylor, M., Athanasopoulou, E., Speyer, O., Raptis, P. I., Marinou, E., Proestakis, E., Solomos, S., Gerasopoulos, E., Amiridis, V., Bais, A., and Kontoes, C.: Dust impact on surface solar irradiance assessed with model simulations, satellite observations and ground-based measurements, Atmos. Meas. Tech., 10, 2435–2453, https://doi.org/10.5194/amt-10-2435-2017, 2017.

Laven, P.: MiePlot, http://www.philiplaven.com/mieplot.htm, last access: 22 January 2018.

Ma, N., Birmili, W., Müller, T., Tuch, T., Cheng, Y. F., Xu, W. Y., Zhao, C. S., and Wiedensohler, A.: Tropospheric aerosol scattering and absorption over central Europe: a closure study for the dry particle state, Atmos. Chem. Phys., 14, 6241–6259, https://doi.org/10.5194/acp-14-6241-2014, 2014.

Markelj, J., Madronich, S., and Pompe, M.: Modeling of hygroscopicity parameter kappa of organic aerosols using quantitative structure-property relationships, J. Atmos. Chem., 74, 357–376, https://doi.org/10.1007/s10874-016-9347-3, 2017.

Mayer, B. and Kylling, A.: Technical note: The libRadtran software package for radiative transfer calculations – description and examples of use, Atmos. Chem. Phys., 5, 1855–1877, https://doi.org/10.5194/acp-5-1855-2005, 2005.

Mehri, T., Kemppinen, O., David, G., Lindqvist, H., Tyynelä, J., Nousiainen, T., Rairoux, P., and Miffre, A.: Investigating the size, shape and surface roughness dependence of polarization lidars with light-scattering computations on real mineral dust particles: Application to dust particles' external mixtures and dust mass concentration retrievals, Atmos. Res., 203, 44–61, https://doi.org/10.1016/j.atmosres.2017.11.027, 2018.

Mie, G.: Beiträge zur Optik trüber Medien, speziell kolloidaler Metallösung, Annalen der Physik, 25, 377–445, https://doi.org/10.1002/andp.19083300302, 1908.

Mishchenko, M. I. and Travis, L. D.: Capabilities and limitations of a current Fortran implementation of the T-Matrix method for randomly oriented, rotationally symmetric scatterers, J. Quant. Spectrosc. Ra., 60, 309–324, https://doi.org/10.1016/S0022-4073(98)00008-9, 1998.

Mishchenko, M. I. and Yurkin, M. A.: On the concept of random orientation in far-field electromagnetic scattering by nonspherical particles, Opt. Lett., 42, 494–497, https://doi.org/10.1364/OL.42.000494, 2017.

Mishchenko, M. I., Travis, L. D., Kahn, R. A., and West, R. A.: Modeling phase functions for dustlike tropospheric aerosols using a shape mixture of randomly oriented polydisperse spheroids, J. Geophys. Res., 102, 16831–16847, https://doi.org/10.1029/96JD02110, 1997.

Mishchenko, M. I., Travis, L. D., and Lacis, A. A.: Scattering, Absorption, and Emission of Light by Small Particles, Cambridge University Press, 2002.

Mishchenko, M. I., Geogdzhayev, I. V., and Yang, P.: Expansion of tabulated scattering matrices in generalized spherical functions, J. Quant. Spectrosc. Ra., 183, 78–84, https://doi.org/10.1016/j.jqsrt.2016.05.015, 2016.

Müller, D., Lee, K.-H., Gasteiger, J., Tesche, M., Weinzierl, B., Kandler, K., Müller, T., Toledano, C., Otto, S., Althausen, D., and Ansmann, A.: Comparison of optical and microphysical properties of pure Saharan mineral dust observed with AERONET Sun photometer, Raman lidar, and in situ instruments during SAMUM 2006, J. Geophys. Res.-Atmos., 117, D07211, https://doi.org/10.1029/2011JD016825, 2012.

Müller, D., Böckmann, C., Kolgotin, A., Schneidenbach, L., Chemyakin, E., Rosemann, J., Znak, P., and Romanov, A.: Microphysical particle properties derived from inversion algorithms developed in the framework of EARLINET, Atmos. Meas. Tech., 9, 5007–5035, https://doi.org/10.5194/amt-9-5007-2016, 2016.

Müller, T., Laborde, M., Kassell, G., and Wiedensohler, A.: Design and performance of a three-wavelength LED-based total scatter and backscatter integrating nephelometer, Atmos. Meas. Tech., 4, 1291–1303, https://doi.org/10.5194/amt-4-1291-2011, 2011.

Otto, S., Bierwirth, E., Weinzierl, B., Kandler, K., Esselborn, M., Tesche, M., Schladitz, A., Wendisch, M., and Trautmann, T.: Solar radiative effects of a Saharan dust plume observed during SAMUM assuming spheroidal model particles, Tellus B, 61, 270–296, https://doi.org/10.1111/j.1600-0889.2008.00389.x, 2009.

Otto, S., Trautmann, T., and Wendisch, M.: On realistic size equivalence and shape of spheroidal Saharan mineral dust particles applied in solar and thermal radiative transfer calculations, Atmos. Chem. Phys., 11, 4469–4490, https://doi.org/10.5194/acp-11-4469-2011, 2011.

Pappalardo, G., Amodeo, A., Apituley, A., Comeron, A., Freudenthaler, V., Linné, H., Ansmann, A., Bösenberg, J., D'Amico, G., Mattis, I., Mona, L., Wandinger, U., Amiridis, V., Alados-Arboledas, L., Nicolae, D., and Wiegner, M.: EARLINET: towards an advanced sustainable European aerosol lidar network, Atmos. Meas. Tech., 7, 2389–2409, https://doi.org/10.5194/amt-7-2389-2014, 2014.

Petters, M. D. and Kreidenweis, S. M.: A single parameter representation of hygroscopic growth and cloud condensation nucleus activity, Atmos. Chem. Phys., 7, 1961–1971, https://doi.org/10.5194/acp-7-1961-2007, 2007.

Petty, G. W. and Huang, W.: The Modified Gamma Size Distribution Applied to Inhomogeneous and Nonspherical Particles: Key Relationships and Conversions, J. Atmospheric Sci., 68, 1460–1473, https://doi.org/10.1175/2011JAS3645.1, 2011.

Piller, N. B. and Martin, O. J. F.: Increasing the performance of the coupled-dipole approximation: a spectral approach, IEEE T. Antenn. Propag., 46, 1126–1137, https://doi.org/10.1109/8.718567, 1998.

Polo, J., Ballestrín, J., and Carra, E.: Sensitivity study for modelling atmospheric attenuation of solar radiation with radiative transfer models and the impact in solar tower plant production, Sol. Energ., 134, 219–227, https://doi.org/10.1016/j.solener.2016.04.050, 2016.

Prahl, S.: Mie Scattering Calculator, http://omlc.org/calc/mie_calc.html, last access: 22 January 2018.

Psichoudaki, M., Nenes, A., Florou, K., Kaltsonoudis, C., and Pandis, S. N.: Hygroscopic properties of atmospheric particles emitted during wintertime biomass burning episodes in Athens, Atmospheric Environ., 178, 66–72, https://doi.org/10.1016/j.atmosenv.2018.01.004, 2018.

Querol, X., Alastuey, A., Ruiz, C., Artiñano, B., Hansson, H., Harrison, R., Buringh, E., ten Brink, H., Lutz, M., Bruckmann, P., Straehl, P., and Schneider, J.: Speciation and origin of PM10 and PM2.5 in selected European cities, Atmos. Environ., 38, 6547–6555, https://doi.org/10.1016/j.atmosenv.2004.08.037, 2004.

Schumann, U., Mayer, B., Gierens, K., Unterstrasser, S., Jessberger, P., Petzold, A., Voigt, C., and Gayet, J.-F.: Effective Radius of Ice Particles in Cirrus and Contrails, J. Atmos. Sci., 68, 300–321, https://doi.org/10.1175/2010JAS3562.1, 2011a.

Schumann, U., Weinzierl, B., Reitebuch, O., Schlager, H., Minikin, A., Forster, C., Baumann, R., Sailer, T., Graf, K., Mannstein, H., Voigt, C., Rahm, S., Simmet, R., Scheibe, M., Lichtenstern, M., Stock, P., Rüba, H., Schäuble, D., Tafferner, A., Rautenhaus, M., Gerz, T., Ziereis, H., Krautstrunk, M., Mallaun, C., Gayet, J.-F., Lieke, K., Kandler, K., Ebert, M., Weinbruch, S., Stohl, A., Gasteiger, J., Groß, S., Freudenthaler, V., Wiegner, M., Ansmann, A., Tesche, M., Olafsson, H., and Sturm, K.: Airborne observations of the Eyjafjalla volcano ash cloud over Europe during air space closure in April and May 2010, Atmos. Chem. Phys., 11, 2245–2279, https://doi.org/10.5194/acp-11-2245-2011, 2011b.

Szymanski, W. W., Nagy, A., and Czitrovszky, A.: Optical particle spectrometry – Problems and prospects, J. Quant. Spectrosc. Ra., 110, 918–929, https://doi.org/10.1016/j.jqsrt.2009.02.024, 2009.

Twomey, S.: Introduction to the Mathematics of Inversion in Remote Sensing and Indirect Measurements, Dover Publications, Mineola, New York, 1977.

Valery, A., Cartwright, R., Fausett, E., Ossipov, A., Pasko, E., and Savchenko, V.: HyperFun project: a framework for collaborative multidimensional F-rep modeling, Eurographics/ACM SIGGRAPH Workshop Implicit Surfaces '99, Bordeaux, France, 1999.

van de Hulst, H. C.: Light Scattering by Small Particles, Dover Publications, New York, 1981.

Vogel, A., Diplas, S., Durant, A. J., Azar, A. S., Sunding, M. F., Rose, W. I., Sytchkova, A., Bonadonna, C., Krüger, K., and Stohl, A.: Reference data set of volcanic ash physicochemical and optical properties, J. Geophys. Res.-Atmos., 122, 9485–9514, https://doi.org/10.1002/2016JD026328, 2017.

Weinzierl, B., Petzold, A., Esselborn, M., Wirth, M., Rasp, K., Kandler, K., Schütz, L., Koepke, P., and Fiebig, M.: Airborne measurements of dust layer properties, particle size distribution and mixing state of Saharan dust during SAMUM 2006, Tellus B, 61, 96–117, https://doi.org/10.1111/j.1600-0889.2008.00392.x, 2009.

Weinzierl, B., Sauer, D., Minikin, A., Reitebuch, O., Dahlkötter, F., Mayer, B., Emde, C., Tegen, I., Gasteiger, J., Petzold, A., Veira, A., Kueppers, U., and Schumann, U.: On the visibility of airborne volcanic ash and mineral dust from the pilot's perspective in flight, Phys. Chem. Earth, 45, 87–102, https://doi.org/10.1016/j.pce.2012.04.003, 2012.

Wiegner, M., Gasteiger, J., Kandler, K., Weinzierl, B., Rasp, K., Esselborn, M., Freudenthaler, V., Heese, B., Toledano, C., Tesche, M., and Althausen, D.: Numerical simulations of optical properties of Saharan dust aerosols with emphasis on lidar applications, Tellus B, 61, 180–194, https://doi.org/10.1111/j.1600-0889.2008.00381.x, 2009.

Wiegner, M., Gasteiger, J., Groß, S., Schnell, F., Freudenthaler, V., and Forkel, R.: Characterization of the Eyjafjallajökull ash-plume: Potential of lidar remote sensing, Phys. Chem. Earth, 45–46, 79–86, https://doi.org/10.1016/j.pce.2011.01.006, 2012.

Wiegner, M., Madonna, F., Binietoglou, I., Forkel, R., Gasteiger, J., Geiß, A., Pappalardo, G., Schäfer, K., and Thomas, W.: What is the benefit of ceilometers for aerosol remote sensing? An answer from EARLINET, Atmos. Meas. Tech., 7, 1979–1997, https://doi.org/10.5194/amt-7-1979-2014, 2014.

Yang, P., Feng, Q., Hong, G., Kattawar, G. W., Wiscombe, W. J., Mishchenko, M. I., Dubovik, O., Laszlo, I., and Sokolik, I. N.: Modeling of the scattering and radiative properties of non-spherical dust-like aerosols, J. Aerosol Sci., 38, 995–1014, https://doi.org/10.1016/j.jaerosci.2007.07.001, 2007.

Yurkin, M. A. and Hoekstra, A. G.: The discrete-dipole-approximation code ADDA: Capabilities and known limitations, J. Quant. Spectrosc. Ra., 112, 2234–2247, https://doi.org/10.1016/j.jqsrt.2011.01.031, 2011.

Yurkin, M. A., Min, M., and Hoekstra, A. G.: Application of the discrete dipole approximation to very large refractive indices: Filtered coupled dipoles revived, Phys. Rev. E, 82, 036703, https://doi.org/10.1103/PhysRevE.82.036703, 2010.

Zhang, Y., Easter, R. C., Ghan, S. J., and Abdul-Razzak, H.: Impact of aerosol size representation on modeling aerosol-cloud interactions, J. Geophys. Res.-Atmos., 107, AAC 4-1–AAC 4-17, https://doi.org/10.1029/2001JD001549, 2002.

Zhuang, B., Wang, T., Liu, J., Che, H., Han, Y., Fu, Y., Li, S., Xie, M., Li, M., Chen, P., Chen, H., Yang, X.-Q., and Sun, J.: The optical properties, physical properties and direct radiative forcing of urban columnar aerosols in the Yangtze River Delta, China, Atmos. Chem. Phys., 18, 1419–1436, https://doi.org/10.5194/acp-18-1419-2018, 2018.

Zieger, P., Fierz-Schmidhauser, R., Weingartner, E., and Baltensperger, U.: Effects of relative humidity on aerosol light scattering: results from different European sites, Atmos. Chem. Phys., 13, 10609–10631, https://doi.org/10.5194/acp-13-10609-2013, 2013.

Zieger, P., Fierz-Schmidhauser, R., Poulain, L., Müller, T., Birmili, W., Spindler, G., Wiedensohler, A., Baltensperger, U., and Weingartner, E.: Influence of water uptake on the aerosol particle light scattering coefficients of the Central European aerosol, Tellus B, 66, 22716, https://doi.org/10.3402/tellusb.v66.22716, 2014.